Norges miljø- og
biovitenskapelige
universitet

Master's Thesis 2019 60 ECTS
Faculty of Science and Technology

The effect of Losartan treatment assessed using magnetic resonance imaging of human tumour xenografts

Simen Rykkje Grønningsæter
Environmental Physics and Renewable Energy

Preface

This thesis was written at the Department of Radiation Biology, Institute of Cancer Research, the Norwegian Radium Hospital.

I want to thank Jon-Vidar Gaustad for his guidance and continuous help during the master thesis, and to Einar K. Rofstad for his guidance during the weekly meetings. I would also like to thank the rest of research group for all of their advice and for making this a lovely year.

I want to thank Cecilia M. Futsæther for all of her advice and proofreading.

Lastly, I want to thank Nicoline Sofie Grepperud. Her support and patience during the last year is highly appreciated. Honourable mentions to her and all my friends at NMBU who have made these past years as a student memorable and fun.

Abstract

This study investigates the possibility of using the angiotensin-II-receptor-blocker (ARB) Losartan to increase oxygenation in tumours. Reduced blood flow in tumours restricts the delivery of oxygen, nutrients and pharmaceuticals. Oxygen deprivation causes hypoxia, which not only reduces the efficacy of radio-, immuno-, and chemotherapy, but also induces tumour progression and metastasis. Tumours that contain high levels of fibrosis, show reduced blood flow as a result of solid stress compressing vessels in the tumour. The solid stress is a result of proliferating tumour cells and contraction forces caused by the fibrous content.

Losartan is commonly used for treating hypertension, but is also shown to have antifibrotic effects. By decreasing fibrous content, such as collagen I, it has previously been shown that Losartan should relieve solid stress in tumours. Relieving solid stress in the tumour micro-environment increases the number of perfused vessels and reoxygenate tissue.

To examine the effect of Losartan, human cancer cell lines CK-160 (Squamous cell cervical carcinoma) and Capan-2 (Pancreatic ductal adenocarcinoma) were inserted into athymic adult female Balb/c-*nu/nu* mice. The mice were given a daily treatment of 30 mg/kg Losartan (Losartan group) or the equivalent volume of pure PBS (vehicle group). The treatment effect was assessed by magnetic resonance imaging (MRI) and immunohistochemistry. Dynamic contrast enhanced magnetic resonance imaging (DCE-MRI) was used to estimate the physiological parameters K^{trans} and v_e. K^{trans} reflect blood flow in tumours and v_e reflects interstitial volume fraction. Diffusion weighted magnetic resonance imaging (DW-MRI) was used to measure diffusion in the tumours, reflected by the Apparent Diffusion Coefficient (ADC). DCE-MRI and DW-MRI were carried out using a 7.05 T bore magnet. Immunohistochemistry was used to determine the fraction of hypoxia, collagen I and connective tissue, and necrosis.

In tumours of the cervical cancer model, CK-160, Losartan treatment did not increase values of K^{trans} ($P > 0.05$), implying that Losartan did not improve blood flow. There was no reduction in hypoxia ($P > 0.05$), but Losartan reduced the amount of necrotic tissue in the tumours ($P = 0.03$). There was no reduction in collagen I content ($P > 0.05$) for Losartan treated mice, which was reflected by an absence of increase in ADC ($P > 0.05$). Losartan did not improve oxygenation in CK-160 tumours.

Losartan treated Capan-2 tumours showed a significant reduction in hypoxic fraction ($P = 0.0011$). The reduction of hypoxia was not due to an increase in blood flow, since Losartan treated tumours also showed a reduction in K^{trans} ($P = 0.0013$). The reduction in perfusion was not reflected by the connective tissue content, showing no significant difference between the Losartan treated and non-treated tumours ($P > 0.05$). Capan-2 tumours did not contain any areas of necrosis. There

were clear indications that Losartan increased oxygenation in Capan-2 tumours, but this increase was not a result of an increase in blood flow. This implies that other mechanisms appear to be responsible for the increase in oxygenation. Further investigations are required to identify these mechanisms.

Losartan increased oxygenation in Capan-2 tumours, but not in CK-160 tumours.

Abbreviations

AIF	Arterial Input Function
ARB	Angiotensin-II-Receptor Blocker
AT1	Angiotensin-II-Receptor 1
AT2	Angiotensin-II-Receptor 2
ATP	Adeno Tri Phosphate
CAF	Cancer Associated Fibroblasts
DCE-MRI	Dynamic Contrast Enhanced Magnetic Resonance Imaging
DICOM	Digital Imaging and Communication in Medicine
DW-MRI	Diffusion Weighted Magnetic Resonance Imaging
ECM	Extracellular Matrix
EES	Extravascular Extracellular Space
FID	Free Induction Decay
FOV	Field of View
FSE	Fast Spin Echo
Gd-DOTA	1,4,7,10-Tetraazacyclododecane-1,4,7,10-tetraacetic acid
Hct	Hematocrit
HE	Hematoxylin and Eosin
i.p.	Intraperitoneally
MRI	Magnetic Resonance Imaging
PBS	Phosphate Buffered Saline
PDAC	Pancreatic Ductal Adenocarcinoma
PIM	Pimonidazole
RAS	Renin Angiotensin System

RF-pulse	Radio Frequency pulse
ROI	Region of Interest
TSP-1	Thrombospondin-1
TGF- β**1**	Transforming Growth Factor -β1
TME	Tumour Micro-Environment
SPGR	Spoiled Gradient Echo

Symbols

α	Flip angle
γ	Gyromagnetic ratio
Δ	Diffusion time
δ	Diffusion gradient duration
$\Delta\omega$	Bandwidth of magnetic field for selecting slice thickness
ρ	Proton density
ρ_t	Tissue density
τ	Optimal slice-selective gradient duration
ADC	Apparent diffusion coefficient $[mm^2/s]$
$\vec{B}_0$	Static magnetic field
$\vec{B}_1$	Magnetic field applied during RF-pulse
$\vec{B}_{eff}$	The effective magnetic field, including gradients
$b-value$	Decides the diffusion weighting in a DWI sequence $[s/mm^2]$
C_t	Concentration of contrast fluid in tissue
C_p	Concentration of contrast agent in arterial plasma
K^{trans}	Volume transfer constant between blood plasma and EES $[min^{-1}]$
$\vec{M}$	Macroscopic magnetisation vector
M_z	Macroscopic longitudinal magnetisation
$M_{x,y}$	Macroscopic transverse magnetisation
M_0	Macroscopic equilibrium magnetisation
R_1	T_1 relaxation rate after arrival of contrast fluid
R_1^0	T_1 relaxation rate before arrival of contrast fluid
r_1	Relaxivity of contrast agent
S	Signal intensity in MRI imaging
S_0	Constant depending on scanner gain and proton density

T_1	Longitudinal relaxation time
T_2	Transverse relaxation time
T_2^*	Transverse relaxation time for observed transverse decay
TE	Echo time
TR	Repetition time
v_e	Fractional volume of EES per volume of tissue
Δz	Slice thickness

Contents

List of Figures

List of Tables

Chapter 1

Introduction

> For every complex problem there is an answer that is clear, simple, and wrong.
>
> *H. L. Mencken*

The idea of finding a single cure for cancer has been discarded but the complexity and variety of the mechanisms involved in treating cancer are still underestimated. Cancer appears in various forms with differences between individuals, between organs, between tumours and even within tumours [30]. The World Health Organisation published that 18.1 million people were diagnosed with cancer worldwide in 2018. 9.6 million succumbed from cancer the same year [52]. While one in six develop cancer worldwide, one in 10 is also likely to die from the disease. The vast variations in cancer types are also reflected by the vast diversity in the frequency of various cancer types and the prognosis of the disease. Two types of cancer that unfortunately have poor prognosis are pancreatic ductal adenocarcinoma (PDAC) and late stages of the cervical squamous cell carcinoma [35][41].

Carcinomas, sarcomas, leukemia and lymphoma are four main categories of cancer. Carcinomas is the cancer of epithelial cells and is the most common form of human cancer [1]. Cervical squamous cell carcinoma is a cancer starting in a type of thin, flat cells in the outer parts of the cervix. It is the fourth leading cause of cancer related death among women [5]. Even though it has good prognosis in its early stages, with a five year survival rate of 80-90%, it gets gradually more difficult to treat in later stages, with the survival rate decreasing down to 25-35% [35]. As it is highly related to the human papilloma virus (HPV), its primary prevention is vaccination [5]. Several countries have also introduced screening programs of women from a young age to discover the disease in an early stage. Despite the advances in prevention and screening it remains a life-threatening disease worldwide [24]. For those who have already developed the disease, the two main choices of treatment is surgery and chemo-radiotherapy.

Adenocarcinoma is a type of epithelial cancer that originates in glandular tissue [1]. The pancreas is responsible for producing hormones, e.g. insulin, in the pancreatic islands. It produces several digestive enzymes, bicarbonate ion and ducts in the pancreatic tissue surrounding these islands. Pancreatic ductal adenocarcinoma (PDAC) is a type epithelial tumour that arises from the cells of the pancreatic duct [41]. PDACs usually lack symptoms at its early stage and is therefore often not discovered before it is too late to cure [38]. Pancreatic cancer had 458918 new cases and caused 432242 deaths worldwide in 2018, where 85% of these were PDACs.

The prognosis of PDAC is also poor, with a five year survival rate of just 9% [38]. The only chance for cure today is surgery, but 80-90% of PDAC patients are unresectable. The risk factors include, amongst several others, diabetes and obesity [41]. There has been an increase in diabetes worldwide from 4.7% in 1980 to 8.5% in 2014 [8]. There is also a significant increase in obesity with countries more than doubling the percentage of overweight and obese. Some countries have an obese percentage of more than 70% of the adult population. Worldwide the number of obese has outgrown the number of underweight [8]. With both diabetes and obesity becoming increasing problems worldwide, finding decent treatments to PDAC could be of great importance.

Low blood flow is a common trait in tumours [30]. This leads to insufficient delivery of oxygen, nutrients and pharmaceuticals, which has negative consequences in cancer treatment. Oxygen is important for the energy extraction in the cells, and when there is an imbalance between oxygen consumption and oxygen supply, tissue becomes hypoxic [1][15]. Hypoxia creates an unfavourable environment for cells, and has been shown to be a driver of tumour aggressiveness, progression and metastasis [30]. Additionally, hypoxic tumours show an increased resistance towards therapies such as radiotherapy, immunotherapy and chemotherapy [30]. Finding methods to improve blood flow in tumours, and thereby decrease the levels of hypoxia, could potentially result in improved patient outcome for several cancer types.

One common property of tumours is high levels of fibrous contents [30]. The high levels of fibrous components such as collagen I and hyaluronan have been shown to correlate with reduced levels of blood flow [9]. High levels of fibrous content increase tumour stiffness and when the tumour cells proliferate, the pressure increases. The increased pressure compresses vessels and reduces blood flow [30]. Reducing collagen I and hyaluronan could therefore be a key to increase tumour blood flow.

A study by Chauhan et al. [9] is one of several studies showing the promise of Losartan, an angiotensin-II-receptor-blocker, in treating highly fibrotic tumours. Losartan, is commonly used to treat hypertension, but has been shown to also have antifibrotic properties. Chauhan et al. [9] showed that Losartan reduced collagen I, thereby reducing mechanical stress and increasing blood flow in breast and pancreatic cancer models. They also showed that collagen I was the most important component for improving blood flow. Other studies have also shown a reduction in collagen and increased perfusion with the use of Losartan for breast and pancreatic cancer models, as well as ovarian and skin cancer [13][26][43][53]. Losartan also improved efficacy of various cancer treatments in these studies.

The aim of this study was to investigate if Losartan would have an effect in a cervical cancer model and a PDAC model. For this, the cervical cancer model CK-160 and the PDAC model Capan-2 were chosen. Both CK-160 and Capan-2 have been shown to contain substantial levels of collagen I and hypoxia [16][25][48][49]. The cancer models should therefore be suitable for measuring the effect of Losartan. If Losartan can improve oxygenation in tumour models CK-160 and Capan-2, it could potentially improve the effect of cancer therapies and thereby the outcome of patients.

A xenograft is a transplant from one species to another, and is commonly used in cancer studies to investigate tumours response to treatments [22]. This study used human cell lines of CK-160 and Capan-2 injected to athymic mice where the cancer cells developed into tumour xenografts. The collagen I content and degree of hypoxia in the tumours was estimated using immunohistochemistry.

This study also use magnetic resonance imaging (MRI) to evaluate the physiological conditions of tumours and tumour response to Losartan treatment. Dynamic contrast enhanced magnetic resonance imaging (DCE-MRI) studies the uptake of contrast agent, which is dependent on blood flow, permeability in blood vessels and the extravascular extracellular space (EES) [15]. By using the Tofts pharmacokinetic model, the physiological parameters K^{trans} and v_e were determined. K^{trans} reflects perfusion in tumours, where perfusion is the flow of blood per unit mass of tissue. v_e reflects the extravascular extracellular space. Diffusion weighted imaging (DW-MRI) was used to estimate the parameter apparent diffusion coefficient (ADC), which can be used to estimate the fibrous content in tumours [23].

The following study wants to investigate if Losartan increases oxygenation in CK-160 and Capan-2 tumours, by reducing collagen I and thereby increasing perfusion. This is done by measuring hypoxia with immunohistochemistry, perfusion with DCE-MRI, and collagen and connective tissue content with both DW-MRI and immunohistochemistry.

Chapter 2

Theory

2.1 Xenografts

A xenograft is a transplant, e.g. tissue, from one species inserted into another [22]. In the field of cancer research, it is common to make use of human tumour xenografts inserted into mice, allowing the tumour to grow and be observed *in situ*. A problem is that the immune system of the host animal will attack the foreign cells and the host animals are therefore bred to lack a normal immune system.

Nude mice, also known as athymic mice, are immunodeficient and can be used as hosts for xenografts [42]. As the name athymic suggests, the thymus of the mice is absent. This results in a inhibited immune system and a reduction in T-cells, which are developed in the thymus [1][42]. T-cells act directly, either by killing a virus infected host cell or by producing a signal molecule activating macrophages. These macrophages can destroy the marked invading microbes [1].

Since the mice lack T-cells, it is possible to establish foreign tissue growth without being attacked by the host immune system [42]. However, the mice are not completely immunodeficient and do contain B-cells, which are developed in the bone marrow, and Natural Killer cells (NK-cells) [1][42]. NK-cells are a part of the innate immune system, and forces their target to commit suicide [1]. The activity of NK-cells reduces the percentage of successfully engrafted tumours [42].

There are challenges using the xenografts in mice. Stromal and vascular tissue in the tumours are of mice origin, which can affect the tumours response to treatment [22]. Xenografts do, however, maintain several of the same response characteristics as the original human tumour. The fraction of hypoxic cells are much the same as normal tumours found in humans and the xenografts maintain the common chemotherapeutic response characteristics as their class of tumour [22]. The xenografts show individual response to treatment, despite essentially being genetically identical [22]. Xenografts have a doubling time one fifth of the doubling time observed in humans, which reduces the length of the study.

2.2 Tumour physiology

Tumour micro-environment

Tumours differ in proliferation, vascularity, inflammation, invasiveness and desmoplasia, not just between tumours but also between the sub-populations of individual tumours [30]. The cancer cells interact with the host cells and creates a tumour micro-environment (TME) that consist of cancer cells, stromal cells, vessels and the extracellular matrix. Stroma is the part of tissue or organ responsible for functional and structural support to the parenchyma, which is the part of tissue responsible for organ specific tasks [30]. The stroma consists of fibroblasts, immune cells and endothelial cells and these cells are recruited by cancer cells in tumours [1][30]. The extracellular matrix (ECM) is important for structure in tissue and consists of a complex network of polysaccharides and proteins which encloses the tumour space [1][30].

2.2.1 Hypoxia

The TME is nourished by blood vessels and drained by lymphatic vessels. The delivery of oxygen, nutrients and therapeutic agents depends on vessel flow and can therefore play a central role in both the development of tumours and the efficacy of treatment [9][30].

A common trait in tumours is reduced blood flow [30]. The amount of blood flow per unit mass of tissue is referred to as perfusion [7]. A reduction in perfusion decrease the amount of oxygen, nutrients and pharmaceuticals delivered to the cells. This reduces the efficacy of cancer therapies that use blood flow to deliver drugs. A reduction in delivered oxygen causes hypoxia.

Cells require a constant supply of energy to maintain the biological order that keeps them alive [1]. Energy is obtained by splitting a glucose molecule into two pyruvate molecules in the cytosol, before continuing in the mitochondria with the citric acid cycle and various others processes. The result of these processes are 32 ATPs and some waste products. ATP, Adinosin Tri Phosphate, is the main energy carrier of the cells. For this process to happen oxygen is essential, and is why it is called aerobic metabolism [1].

In the absence of oxygen, which is the case for hypoxia, the cell makes use of the anaerobic metabolism. In this situation, pyruvate stay in the cytosol and is converted into lactate to produce energy in the form of two ATPs [1]. The acidic environment caused by the lactic acid byproduct from anaerobic metabolism, is problematic for the cells and causes the cancer cells to migrate. Hence, when there is insufficient oxygen available, and proliferation is promoted at the expense of energy efficiency, the risk of metastasis is increased.

Cell migration is facilitated by polymerising and regulating the alignment collagen fibres and integrin activity, a process regulated by Hypoxia-Inducible Factor α (HIF-α). HIFs are also responsible for facilitating an increase in vessel permeability which allows metastatic cancer cells to migrate [30]. HIFs are transcriptional factors that regulate the expression of genes relevant for cellular processes such as metabolism, angiogenesis, erythropoiesis, cell proliferation and apoptosis [22].

Hypoxia is shown to reduce efficacy of immunotherapy, chemotherapy and radiotherapy [30]. Most of the damage produced in cells after irradiation is caused by free radicals, and the damage becomes irreversible when oxygen is available. Free radicals forms when oxygen is available and fixates the radiation lesions, making them permanent. The DNA damage inactivates the cells during the next cell cycle, and this is the goal of radiation therapy [22]. For hypoxic regions, the cells are able to repair the damage caused by indirect action. The cancer cells are thereby able to continue proliferating. This is one central reason why hypoxic tumours respond poorly to radiotherapy.

The effects of some chemotherapeutic agents are reduced due to fluctuating blood flow, drug diffusion distance and decreased proliferation. Chemotherapeutic agents which induce DNA damage by exploiting free radicals are less efficient in hypoxic areas since the number of free radicals generated is reduced. Additionally, due to the acidity caused by hypoxia, the activity of some agents are diminished [22].

Necrosis

Necrosis is a common feature of solid tumours in core regions due to oxygen and glucose depletion, and is usually accompanied by ATP-depletion, inflammatory response and the disintegration of cells [37]. Tissue that remain hypoxic, with continuous oxygen deficiency and insufficient energy production, are therefore likely to turn necrotic [14][22].

Necrosis is a way of the cells to end their life cycle that differ from apoptosis. Apoptosis is referred to as programmed cell death and happens in a controlled fashion [14]. It is energy efficient, organised and beneficial for the overall biological system. The nuclei constituents are fragmented and sorted before they are recognised and removed by phagocytic cells [14]. During necrosis the organelles swell and the plasma membrane ruptures [33]. Necrosis is therefore often compared to a train wreck and is traditionally thought to be uncontrolled. However, studies show examples of controlled necrosis and several necrotic pathways has been discovered [14][33]. Tumour necrosis factor (TNF) is described as a central component in cases where necrosis is induced instead of apoptosis, and hypoxia is shown to increase the production of TNF-α [14][37].

Proliferating cells which do not have any access to oxygen can not perform glucose metabolism properly. An alternative to glucose metabolism could be fatty acid oxidation, which also results in a higher amounts of ATP per gram. However, proliferating cells can not use amino acids or lipids as fuel either since both amino acids and lips are central when creating cell membranes in new cells. Additionally, fatty acid oxidation requires more oxygen, and glucose metabolism is therefore prioritised when there is insufficient oxygen available [27]. The lack of energy sources available ultimately leads to bio-energetic stress that results in necrosis [14].

Causes of hypoxia

Hypoxia is a result of of an imbalance between oxygen supply and oxygen consumption [15]. This can be caused by high cell density in the tissue, consuming more oxygen than is available. It can also be caused by an insufficient supply of oxygen from the surrounding vessels. This can be due to an obstruction of the vessels in the tissue or due to a large diffusion distance between vessels and cells, preventing oxygen from reaching the cells [22]. Unlike anoxia, where the oxygen levels are too low for the cells to survive, cells are able to survive hypoxia if they are reoxygenated [22].

Cells that lie too far from blood vessels struggle to get enough oxygen and this situation is referred to as chronic hypoxia. Another possibility is that the vessels are compressed, which restricts blood flow and stops oxygen from reaching cells. This is called acute hypoxia and can be reversed by decompressing vessels, allowing blood to flow freely. Chronically hypoxic cells are less likely to be reoxygenated, and is therefore more likely to die and turn necrotic. Both acute and chronic hypoxia have been shown to drive malignant progression [22].

Compared to normal tissue, the generation of blood vessels (angiogenesis) in tumours are often chaotic with highly permeable vessels. This is one mechanism that can cause hypoxia, due to the leakiness of the tumour vessels are bigger than the lymphatic system are able to drain. This turns the interstitial fluid pressure and the microvascular pressure close to equal. The gradient of pressure across the vessel wall is close to zero and the flow of blood containing oxygen, nutrients and drugs are very low[30].

A different cause of hypoxia is a common trait of several cancer forms is high amounts of fibrous content [30]. This leads to increased stiffness in tumours. The combination of fibrous content and tumour cells continuously proliferating, increases the mechanical pressure in tumours and compress the vessels. The compressed vessels are unable to deliver the amount of oxygen that the tumours require, especially with the tumours extensive need for energy. The oxygen consumption outbalance oxygen supply, and the tumours turn hypoxic.

Collagen I and hyaluronan are common constituents in the extracellular matrix

(ECM) and is two central components in tumour fibrosis. The ECM is a network of extracellular macro-molecules that provide structural support in tissue, and influence the development and physiology [1].

2.2.2 Extracellular matrix components

Hyaluronan

Hyaluronan, also known as hyaluronic acid, is a polysaccharide (glucosaminglycan) with negative charge [28][46]. The electrostatic charge of hyaluronan withstands compression stress in tissue, e.g. due to cell proliferation. When the magnitude of compressive stress energy exceeds a certain maximum point, the stress is transmitted to tumour vessels which results in restricted perfusion [9]. However, studies have shown that due its flexibility, high levels of hyaluronan only correlates with reduced perfusion in the ECM when the levels of collagen is high [9]. Hyaluronan also increases interstitial fluid pressure and enhances apoptotic resistance [51].

Interestingly, some studies show that elevated levels of hyaluronan in cancers are linked to tumour aggression and poor outcome whereas others indicate that hyaluronan acts as a stromal tumour suppressor[31]. The reason for this could be linked to the size, or molecular weight, of the hyaluronic acids. Small molecules of hyaluronan fragments and the enzyme hyaluronidase, are produced during tissue stress, repair and chronic disease and are pro-inflammatory and pro-fibrotic [31]. Production of high molecular weight hyaluronan appears to resist oncogenic transformation of fibroblasts in naked mole rats [31]. The precise effect of the hyaluronan size remains unclear.

Collagen

Collagen is a central constituent of the extracellular matrix and connective tissue. It is a protein rich in glycine and proline, that exists in many forms. Collagen I is the most common type and is found in skin, tendon and bone. Collagen I plays a central role in tumour desmoplasia. Type II found in cartilage and type IV found in basal laminae are other examples [1].

Unlike hyaluronan, collagen is correlated with reduced perfusion regardless of hyaluronan levels [9]. Studies have shown that when collagen I is reduced, the solid stress is relieved and perfusion increases [9].

The accumulation of collagen I fibrils in cancerized stroma are cross-linked which leads to an increase of the stromal stiffness and a proteolytic resistance [31]. Proteolysis is the process of breaking down proteins to smaller parts, such as polypeptides and amino acids. Stiffness, proteolytic resistance and the orientation of collagen fibrils promotes tumour cell migration, invasion and proliferation. The orientation of collagen fibrils is used as a biomarker for tumour cell invasion, metastasis and poor outcome [31].

Both hyaluronan and collagen contribute to solid stress in the tumour. Solid stress refers to the mechanical stress caused by solid components of the tumour such as cancer cells, stromal cells and the ECM [46]. Hyaluronan resists compression and collagen resists tension and confines the local micro-environment [9]. The compression of the blood and lymphatic vessels of the tumour reduce perfusion and thereby induce hypoxia [46]. The solid stress can also compress cancer cells and reduce their proliferation rate, thereby increasing their invasiveness and metastatic potential [46].

The combination of high fibrotic content and proliferation is referred to as desmoplasia, and is illustrated in Figure 2.1. The figure shows collagen I, hyaluronan and blood vessels, and the beige background illustrates the various cells. F_c represents the compression forces that arises due to desmoplasia. At a certain point, the pressure surpass what hyaluronan are able to resist, and the vessels are compressed. The compression force is denoted F_v in Figure 2.1. In real tumours, the forces would not be solely parallel like in Figure 2.1, but occur from various directions with various strength. The same goes for the orientation of collagen I content, making the process of compressing vessels a lot more complex.

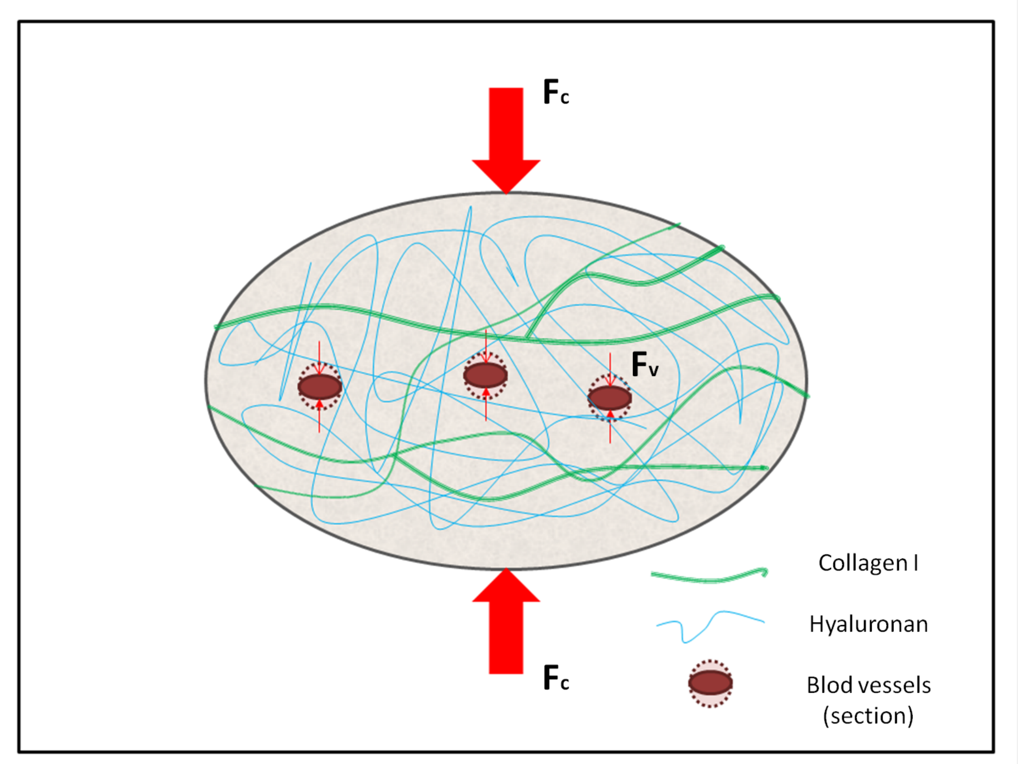

Figure 2.1: The extracellular matrix (ECM) with its fibrous content. The beige background illustrates the tumour cells, and when proliferating they eventually run out of space. This results in a compressing force (F_c) on the tumour ECM from the surrounding tissue. The collagen content shown in green makes the ECM stiff and susceptible for compression, which results in a compression force on blood vessels (F_v) and reduced perfusion. The electrostatic force of the negatively charged hyaluronan, shown in blue, aids the compression.

2.2.3 Cancer and fibroblasts

Cancer cells behave like wounds and forces fibroblasts of the host TME into a state of constant fibrotic repair. This changes the composition and remodels the ECM, creating dense and fibrous tumours [31]. In combination with tumour cells continuously proliferating, the pressure increases within the tumours [30].

Fibroblasts are a common cell type which migrates and proliferates in wounded tissue. They are commonly found in connective tissue and is responsible for producing extracellular matrix components such as collagen and hyaluronan. Fibroblasts recruited by cancer cells are referred to as Cancer-Associated Fibroblasts (CAF). CAFs are a dominant cell type of cancer stroma and their activation appears to be irreversible, in contrast to normal fibroblasts [31]. CAFs also play a significant role in tumour dissemination [31]. A central system in regulating fibroblast activity is Angiotensin-II of the renin angiotensin system (RAS).

Angiotensin

Renin angiotensin system (RAS) is a hormone system responsible for regulating systemic arterial blood pressure and fluid and electrocyte balance. Systemic blood pressure denote that its the blood pressure of the biological system, and not just local pressure in vessels. The RAS is disrupted in several types of cancer possibly due to tissue remodelling, inflammation, angiogenesis and apoptosis [20]. In the simplified illustration of Figure 2.2, we see some of the steps in the RAS. The last part marked orange is central in regard to inflammation and fibrosis. This pathway is the Angiotensin-II-receptor 1 and 2 system, and is often referred to as AT1 and AT2. Receptor 1 and 2 have different roles and the levels of both of them are elevated in CAFs [9]. Angiotensin II promotes angiogenesis and pro-inflammatory RAS-signals, mainly via AT1-receptors.

It has been shown that AT1 when stimulated triggers inflammation and increases oxidative stress, vascular immune dysfunction and hypertension. One of the roles of AT2 is counterbalancing AT1 [2]. When over-expressed, AT1 is typically associated with aggressive tumour features such as larger tumours, higher grade, higher vascular density and poorer outcomes [36]. As Figure 2.2 shows, when AT1 is blocked via down regulating constituents such as thrombospondin-1 (TSP-1) active TGF-β1 is down-regulated. TGF-β1 is a central constituent in pro-fibrotic changes, triggering the production of collagen and hyaluronic acid [30]. In diseased tissue, as is the case for cancer, the over-production of extracellular matrix components is caused by a failed attempt to heal a wound, and results in fibrosis [51].

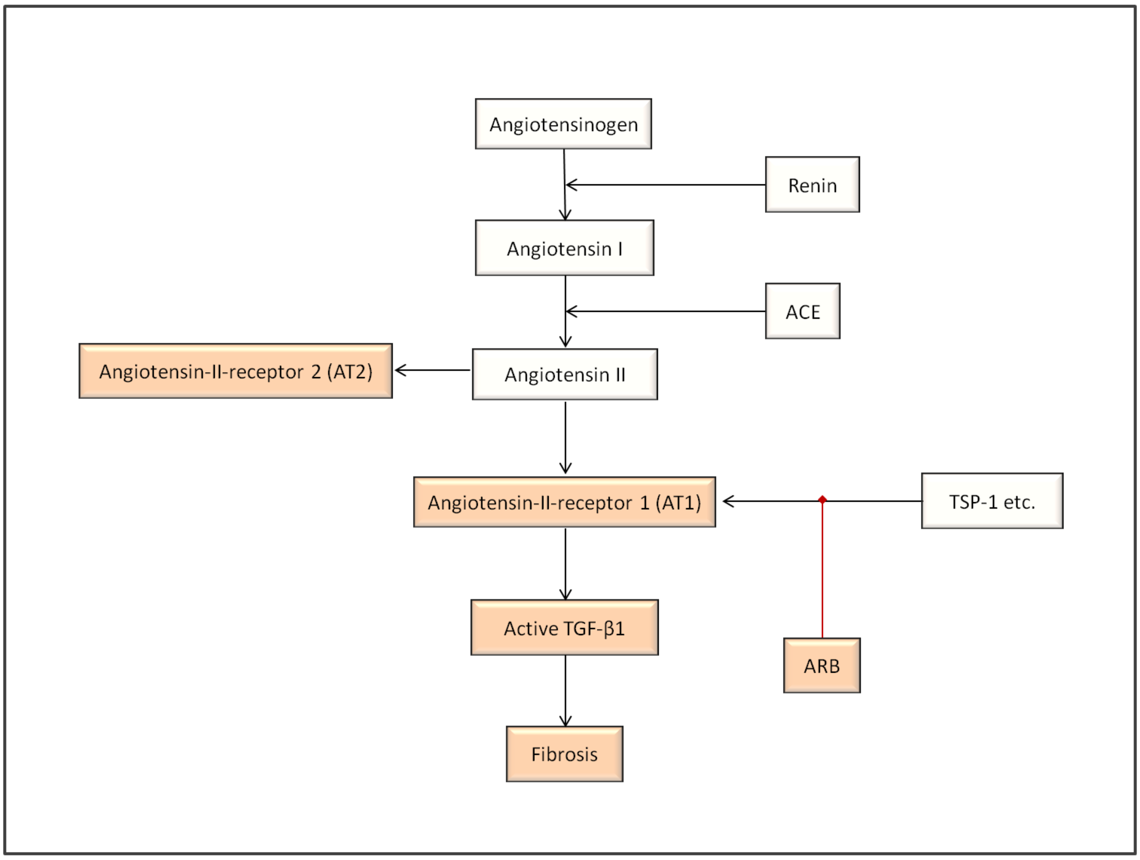

Figure 2.2: Simplified illustration of the Renin-Angiotensin system. The parts coloured orange are central for tumour development in regard to inflammation and fibrosis.

2.3 Losartan

Losartan an Angiotensin receptor blocker (ARB) used as a drug for patients with clinical hypertension, commonly known as high blood pressure. Losartan is approved by the United States of Americas Food and Drug Administration (FDA), have low costs, and is regarded as a safe and effective method for treating hypertension. Since it also effectively penetrates tissues it is the most commonly used ARB [43]. The antifibrotic effects of Losartan is caused by AT1-mediated down regulation of TGF-β1 activators, such as TSP-1, in cancer associated fibroblasts (CAF) [9]. Studies show that Losartan reduces the level of active TGF-β1 by up to 90%, thereby reducing the amount of collagen I and hyaluronan in the tumour micro-environment [13].

Chauhan et al. [9] showed that Losartan increased the amount of perfused vessels, via solid stress relief in tumours by reducing collagen I and hyaluronan content in pancreatic and breast cancer models. Several preclinical studies with mice support this notion. In studies using Losartan for treating breast cancer, Tang et al. [43] showed that it lowered of the collagen I fraction by 53% and enhanced the distribution of oxygenation and delivery of photosensitisers for Photodynamic therapy (PDT).

Zhao et al. [53] showed that by normalising the tumour microenvironment, Losartan increased perfusion, thereby enhancing the distribution and efficacy of chemotherapeutics in ovarian cancer models. Diop-Frimping et al. [13] found similar results for human breast, pancreatic and skin tumours. They also studied the effect of Losartan on nanoparticle penetration, and showed an increase in interstitial transport and delivery of nanotherapeutics n pancreatic adenocarcinoma.

There is no indication that Losartan affects vessel length or density in tumours, but rather that the increased perfusion and permeability of vessels is caused by stress alleviation due to the reduction in intratumoural collagen and hyaluronan level [43]. Losartan is described as an inhibitor of stromal collagen synthesis, but is shown to also reduce hyaluronan content [28][9].

Losartan does not affect levels of metastatic markers E-cadherin and Vimentin, and studies even show a reduction of metastatic incidents in some tumour types [43][13]. Zhao et al. [53] found a reduction in the amount of ascites, a vascular accumulation of the abdominal cavity, in systems where tumours invading diaphragm. When the TME was normalised it also affected the lymphatic network and improved drainage function.

2.4 Magnetic resonance imaging - MRI

Magnetic resonance imaging is a highly complex subject that can be explained by both classical physics and quantum mechanics [7]. To gain full insight into MRI quantum mechanics is needed, but classical theory of electromagnetism can give a sufficient description [47].

2.4.1 A brief description

The magnetic dipole moment of nuclei is central in MRI [47]. The human body consist of up to 70% water resulting in an abundance of hydrogen atoms (protons). Nuclei with an even number of protons and neutrons have no net magnetic dipole, whilst an odd number gives a nonzero magnetic dipole.

The majority of hydrogen atoms on earth only contain one proton, and no neutron, giving them a nonzero magnetic dipole moment. In classical physics this dipole moment arises from movements of protons with a charge $+e$ and an angular momentum $\vec{J}$ which generates a small current i and thus a dipole moment $\vec{\mu}$ [47]. The magnetic dipole moment of a proton is parallel to the rotation axis and proportional to the angular momentum $\vec{J}$:

$$\vec{\mu} = \gamma \vec{J} \tag{2.1}$$

where $\vec{\mu}$ is the magnetic dipole, γ is the gyromagnetic ratio describing the ratio of the magnetic moment to the angular momentum. The gyromagnetic ratio is a constant that is unique for each nuclear isotope possessing a spin [4]. The spin and magnetic moment of these protons are usually random unless they are under external influence.

By placing a system of protons in an external, homogeneous magnetic field, the magnetic moments align with the field. Most of the moments are low-energy nuclei and align parallel to the field. This requires less energy, and is in quantum mechanics referred to as spin-up nuclei. The high-energy nuclei align anti-parallel and is referred to as spin down. The sum of spin of these nuclei is named the net magnetisation vector and reflects the relative balance between spin-up and spin-down nuclei [7].

An external magnetic field $\vec{B}_0$ exerting a force on a magnetic moment $\vec{\mu}$ results in a torque $\vec{\tau}$ acting on the dipole given by

$$\vec{\tau} = \vec{\mu} \times \vec{B}_0 = \frac{d\vec{J}}{dt} \tag{2.2}$$

which in combination with Equation 2.1 gives

$$\frac{d\vec{\mu}}{dt} = \gamma \vec{\mu} \times \vec{B}_0 \tag{2.3}$$

Classically, the proton precesses about the direction of the external field with an angular frequency $\vec{\omega}_L$ as illustrated by Figure 2.4. This frequency is referred to as the Larmour frequency and is given by

$$\vec{\omega}_L = \gamma \vec{B}_0 \tag{2.4}$$

Since the signals from a proton alone are fairly small, MRI makes use of the overall macroscopic magnetisation $\vec{M}$ calculated from the sum of the magnetic moments in each voxel

$$\vec{M} = \frac{1}{V} \Sigma_n \vec{\mu}_i \tag{2.5}$$

where V is the volume containing n protons and $\vec{\mu}_i$ is the contribution from proton number i.

Excitation

As long as the external field is constant, there is little change in the system. By sending a resonant radio frequency pulse (RF-pulse), resonant meaning equivalent to the Larmour frequency, the spinning proton gets pushed out of its equilibrium state and into a higher energy state. The energy difference between spin-up and spin-down populations relates to the energy needed to produce resonance via excitation. If the field strength is increased the difference also increases and higher frequencies are needed to produce resonance [7].

To gain information about $\vec{M}$, the vector needs to be pushed out of the equilibrium orientation parallel to $\vec{B}_0$ [4]. This is done by applying a second magnetic field $\vec{B}_1$, orthogonal to $\vec{B}_0$, during the RF-pulse. This results in a new effective field $\vec{B}_{eff} = \vec{B}_0 + \vec{B}_1 + \Omega/\gamma$. Ω is a rotational vector, with direction opposite to $\vec{B}_0$. $\vec{M}$ will now precess with an angle α away from its position, towards the x, y plane, as illustrated by Figure 2.4. The longer the duration of the RF-pulse, the further away from the equilibrium the magnetisation is pushed. The angle it is pushed is called the flip angle (α). The precessing proton is illustrated by Figure 2.4, with the proton precessing in the transverse plane with an flip angle α

Gradients

By using coils for different directions (x, y and z) a magnetic field gradient is added to $\vec{B}_0$. The centre alongside the gradient axis is called the isocenter and the magnetic field strength is equal to the magnetic field ($\vec{B}_0$). As illustrated by Figure 2.3 the gradient field, $\vec{G}$, either adds or subtracts the external magnetic field strength, typically up to a magnitude of 10^{-2} of $\vec{B}_0$.

With varying strengths of the field, the Larmour frequency varies. A range of RF-pulses is used to match the various Larmour frequencies. At the strong side of the field the nuclei speeds up, and the nuclei slows down at the weak side. Consequently, the gradient can be used to rephase or dephase the magnetic moments [7]. By using gradients in each direction, the magnetic field strength is dependent on direction and placement. The magnetic field strength, $B_z(t)$, in the z-direction at time t is given by

$$\vec{B}_z(t) = \vec{B}_0 + \vec{G}(t)\vec{r} \tag{2.6}$$

where $\vec{r}$ represents position and $\vec{G}$ is the gradient strength [mT/m]. A gradient applied during RF-excitation is referred to as a slice selective gradient [4]. The effective field, $\vec{B}_{eff}$, is then given by

$$\vec{B}_{eff} = \vec{B}_0 + \vec{G}(t)\vec{r} + \vec{B}_1 + \Omega/\gamma = \begin{bmatrix} B_1 \\ 0 \\ B_0 + G_z \Delta z - \Omega/\gamma \end{bmatrix} \tag{2.7}$$

where $\vec{B}_0$ is the magnetic field, parallel to z, $\vec{B}_1$ is a magnetic field applied during the RF-pulse, $\vec{G}(t)\vec{r}$ is the gradient field and Ω is the frequency at a certain position. Usually, instead of a single frequency, Ω, a wide range of frequencies, $\Delta\omega$ is used. By making $B_0 + G_z\Delta z - \Omega/\gamma \gg B_1$, it is possible to create transverse magnetisation in a selected slice without affecting spins outside the given interval. The $\vec{B}_1$-field has a finite band-width $\Delta\omega$ and the width of the slice is given by

$$\Delta z = \frac{\Delta\omega}{\gamma G_z} \tag{2.8}$$

where Δz is the slice thickness and G_z is the gradient along the z-direction. Equation 2.8 show that slices can be made thinner either by increasing gradient G_z or by increasing RF-pulse duration and thereby decreasing $\Delta\omega$. This is illustrated by Figure 2.3, showing a slice selective gradient. The gradient increases as it moves along the z-axis, allowing the use of a range of frequencies in the RF-pulse, $\Delta\omega$, to select a slice of thickness Δz.

Coils placed around object of interest, inside the MR-machine, registers the phase and frequency. Applying gradients in two or three directions gives enough phase information to pinpoint the location of the signal.

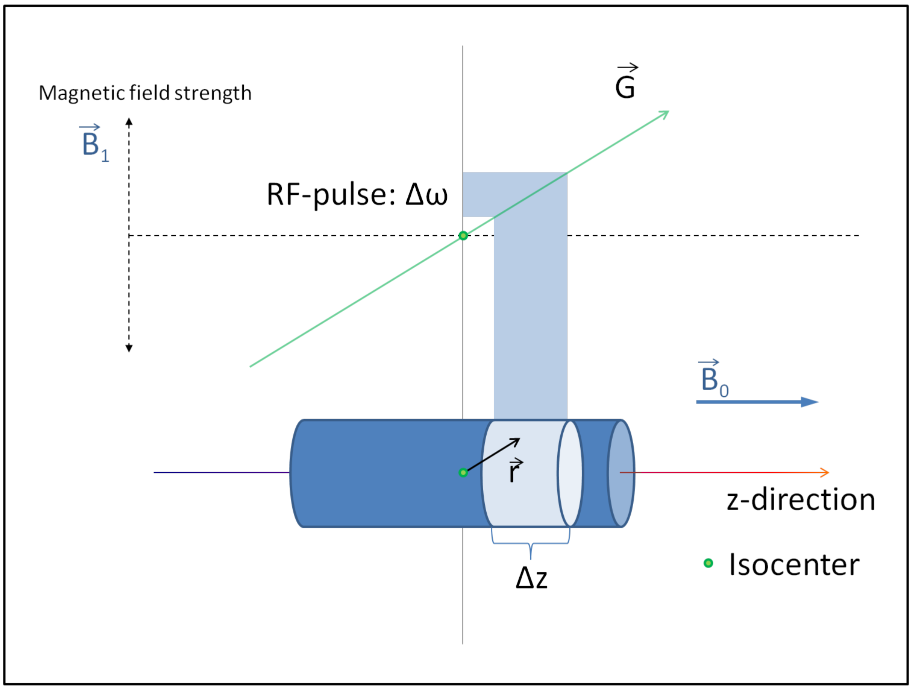

Figure 2.3: Object in a magnetic field consisting of $\vec{B}_0$ and $\vec{B}_1$ with an applied gradient field $\vec{G}$. $\vec{r}$ is a positional vector. The RF-pulse and $\vec{B}_1$ with band-width $\Delta\omega$ is used to excite a slice with width Δz.

Readable signal

As illustrated by Figure 2.4, after the RF-pulse the proton is pushed out of position with an angle α towards the transverse plane. This decreases the M_z and the longitudinal signal. The x, y-component of the magnetisation, $\vec{M}$, is oscillating and can be detected by the induction of a current in a coil placed in the oscillating field. The observed signal due to $M_{x,y}$ is referred to as the MR-signal or free induction decay (FID). The z-component of magnetisation (M_z) do not rotate, and therefore do not induce a current and is not detectable by the coil. After the excitation caused by the RF-pulse, the protons relax back to their equilibrium state, aligned with the external magnetic field $\vec{B}_0$. M_z increases with decreasing $M_{x,y}$ until $\vec{M}$ is aligned $\vec{B}_0$ and $\vec{M} = M_z$. The longitudinal signal is then recovered, and the transverse signal is lost.

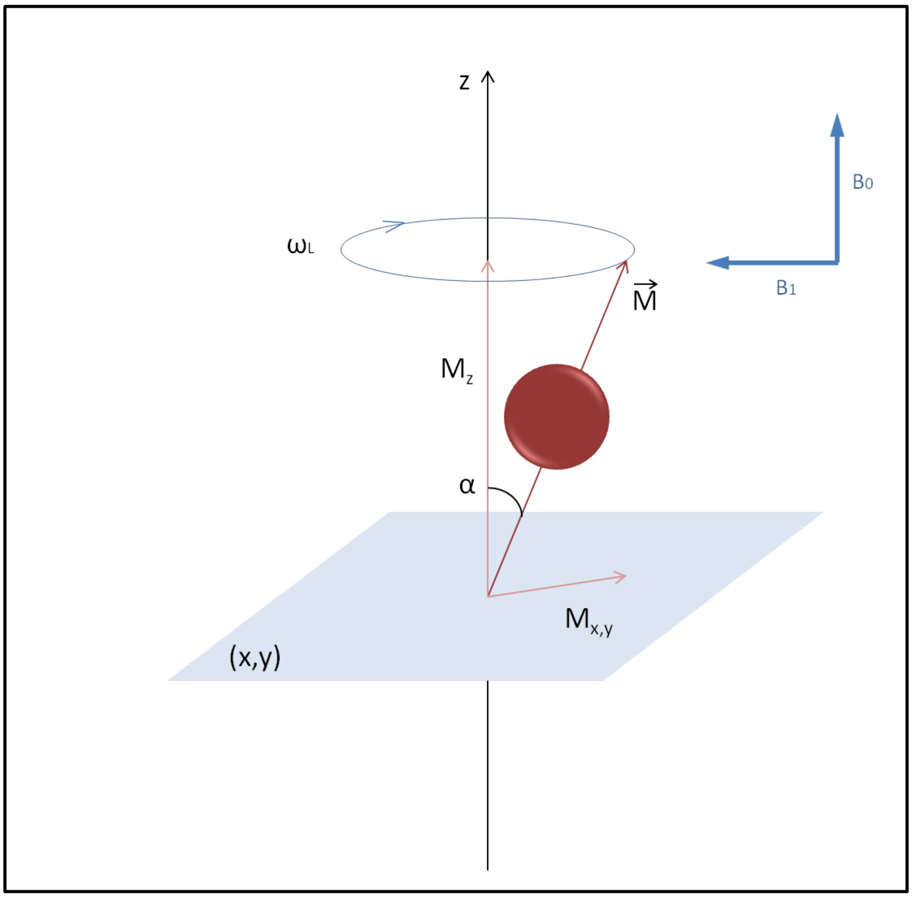

Figure 2.4: Precessing proton with Larmour frequency ω_L, transverse magnetisation $M_{x,y}$, longitudinal magnetisation M_z in an external magnetic field $\vec{B}_0$. T_1 relaxation, or longitudinal relaxation, is described by increasing magnetisation in the z-axis (M_z). T_2/T_2^* dephasing, or transverse relaxation, is described by the decrease of magnetisation in the x,y-plane $(M_{x,y})$. Relaxation rate of T_1 and T_2/T_2^*. The $\vec{B}_1$-field is applied during the RF-pulse.

The FID signal consists of both the frequency and phase. Frequency is the number of times the magnetic moments cross the receiver coils and the phase is their position around their precessional path [7]. This is then stored in a matrix where columns contain information about the frequency and the rows contain information about the phase. The information is thereby stored in a spatial frequency domain, known as k-space, that contain information about the frequency of the signal and the position the signal originates from.

k-space form the basis for the final grey scale image, where the central parts of k-space contain information about the low frequencies giving contrasts, and the outer part containing information about the high spatial frequencies giving details and edges. The frequency information is converted to signal intensity levels by doing a Fourier transform. The Fourier transform is an mathematical operator that allows changes between domains, in terms of a sinusoidal representation. This could for instance be from the frequency domain to the time domain. When converted from frequency domain to signal intensity domain, the signal intensity is displayed as shades of grey.

The size of the spatial encoding area of the two- or three dimensional matrix is known as the field of view (FOV). It is usually in units of $[mm^2]$ and is a squared image area containing information about the object of interest. FOV is inversely proportional to the spacing between samples in the k-space, and in combination with the pixel width determines the number of samples needed to reconstruct the image with the desired resolution.

2.4.2 Relaxation and four important T's

In classical mechanics the changes in macroscopic magnetisation vector $\vec{M}$ resulting from magnetic interactions is described by the Bloch equation:

$$\frac{d\vec{M}}{dt} = \gamma(\vec{M} \times \vec{B}) \tag{2.9}$$

where γ is the gyro-magnetic ratio and $\vec{B}$ is the external magnetic field. The vector describing the rate of change of $\vec{M}$, in Equation 2.9, shows that the magnetic magnetisation vector precesses about the direction of the magnetic field $\vec{B}$. In equilibrium net magnetisation in the transverse plane (x,y) is zero and $\vec{M} = M_z$. This results in pure longitudinal magnetisation ($\vec{M}_z$). As the RF-pulse is applied and pushes $\vec{M}$ out of equilibrium, the magnetisation vector becomes a combination of M_z (longitudinal) and $M_{x,y}$ (transverse) magnetisation. This is illustrated in Figure 2.4, with $\vec{M}$ precessing in the transverse plane. If a flip angle α of 90 ° is applied, the magnetisation vector will precess in the transverse plane and $\vec{M} = M_{x,y}$.

After being excited, the protons relaxes back to equilibrium and the FID signal rapidly decays to zero. The process of excited nuclei releasing energy as they fall from a high to a lower energy state can be characterised by the intrinsic parameters T_1 and T_2, which relates to the relaxation of the spin. T_1 and T_2 affects the imaging sequence by different mechanisms, and the amount of influence caused by the parameters can be regulated by varying operator-selected parameters labelled repetition time (TR) and the echo time (TE). The repetition time TR is the time between two RF-pulses and echo time TE is the time between the RF-pulse and the maximum amplitude of the FID signal induced in the coil.

Spin lattice relaxation describes the process where energy lost to the surroundings returns the magnetic moment towards its original alignment with the external magnetic field. This process is exponential characterised by the T_1 relaxation time, which is the time it takes for 63% of the longitudinal magnitude to recover. Spin-spin relaxation occurs because of interactions between the magnetic fields of neighbouring nuclei which results in the loss of coherent transverse magnetisation. This relaxation is characterised by the T_2 decay constant which is the time it takes for 63% of the transverse magnetisation to be lost.

The T_1 and T_2 relaxation processes are visualised in Figure 2.5. Both T_1 and T_2 relaxation is dependent on the tissue of the precessing protons. It is therefore possible to distinguish tissue from each other based on their relaxation times. The shape of the curves of Figure 2.5 would look different for various tissue.

Whereas T_1 is mainly dependent on the thermal energy of the surrounding tissue, T_2 strongly depends on the density of the surroundings. Both depend on how well the molecular rate of descent matches the Larmour frequency of hydrogen. Small inhomogeneities within the magnetic field that to not match the external magnetic field, give small variations in the Larmour frequency across the body which causes destructive interference that shortens the FID. The time constant for the observed decay of the FID is called T_2^* and is always shorter than T2.

TR decides how much longitudinal relaxation is possible before the next pulse is started, and therefore the amount of T_1 relaxation that has occurred before the signal is read. TE decides the decay in the transverse magnitude and controls the amount of T_2 relaxation that occurs before the signal is read. Both TR and TE are usually in the order of milliseconds. TE and TR is chosen to maximise the difference in obtained relaxation between tissues to achieve optimal contrast in the images.

By using short TR and TE the image is T_1 weighted. Water and fat have different relaxation rates and the signal of fat is higher for T_1 weighted images and will appear brighter. Water will appear dark. The TR needs to be short enough so that neither water nor fat have the time to realign with the external magnetic field.

For T_2 weighted images, with long TR and TE, the transverse magnetic magnitude is larger for water which gives a stronger signal and makes water appear bright. Here, fat will appear dark. T_2 weighted imaging needs TE to be long enough to let both water and fat decay completely to induce a signal [7].

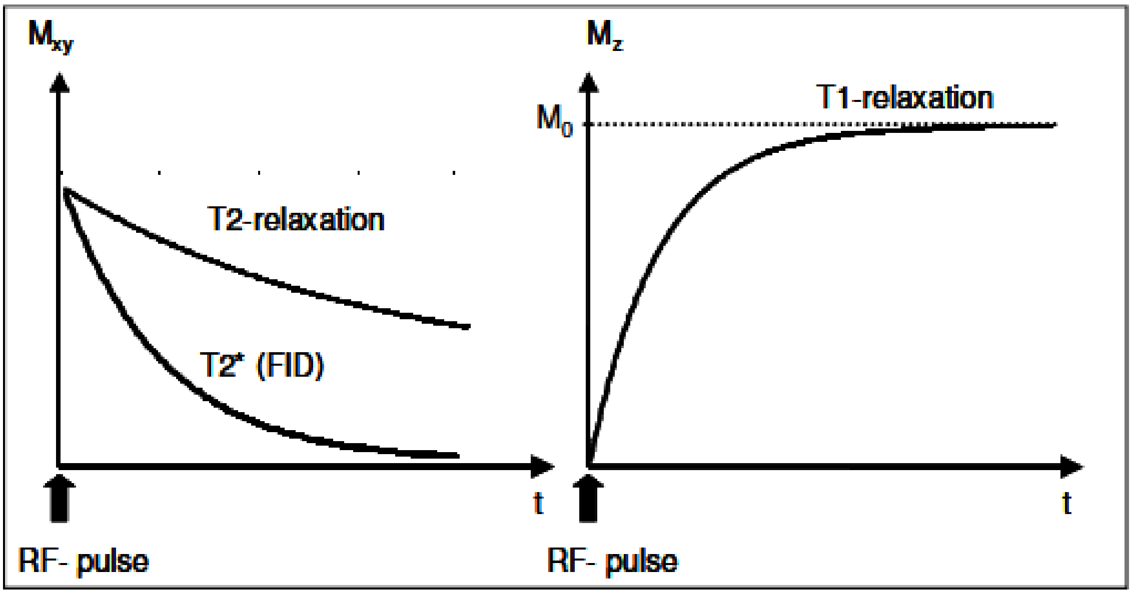

Figure 2.5: Relaxation rate of T_1 and T_2/T_2^*. This figure is borrowed with approval from [4].

The macroscopic relaxation effects consists of M_{xy} gradually disappearing (T_2) and M_z recovering (T_1) after the excitation pulse as illustrated by Figure 2.5. The relaxation process can be described by differential the equations

$$\frac{dM_x}{dt} = -\frac{M_x}{T_2}, \frac{dM_y}{dt} = -\frac{M_y}{T_2}, \frac{dM_z}{dt} = -\frac{M_z - M_0}{T_1} \tag{2.10}$$

M_0 describes the equilibrium magnetisation along the z-axis. This expands the Bloch equation such that it during relaxation can be expressed as

$$\frac{d\vec{M}}{dt} = \gamma \vec{M} \times \vec{B}_{eff} - \vec{R}(\vec{M} - \vec{M}_0) \tag{2.11}$$

where

$$\vec{R} = \begin{bmatrix} \frac{1}{T_2} & 0 & 0 \\ 0 & \frac{1}{T_2} & 0 \\ 0 & 0 & \frac{1}{T_1} \end{bmatrix} \; and \; \vec{M}_0 = \begin{bmatrix} 0 \\ 0 \\ M_0 \end{bmatrix}, \; \vec{M} = \begin{bmatrix} M_x \\ M_y \\ M_z \end{bmatrix} \tag{2.12}$$

and $\vec{B}_{eff}$ is the effective field including $\vec{B}_0$ and gradients, M_0 is the equilibrium magnetisation, and T_1 and T_2 is longitudinal and transverse relaxation times respectively. By solving the differential equation Equation 2.11 we get equation for the development of the transverse (M_{xy}) and the longitudinal signal (M_z):

$$M_z(t) = M_0\left[1 - exp\left(-\frac{t}{T_1}\right)\right] + M_z(0)exp\left(-\frac{t}{T_1}\right) \tag{2.13}$$

$$M_{xy}(t) = M_{xy}(0)exp\left(-\frac{t}{T_2}\right) \tag{2.14}$$

where it is assumed that relaxation effects during the RF-pulse is negligible. The development of the magnetisation relaxation is shown in Figure 2.5.

2.4.3 Magnetisation and signal

When introducing a slice selective gradient to Equation 2.14 and assuming T_2 relaxation effects to be negligible during time t, the total transverse magnetisation can be described by

$$M_{xy} = M_T(\vec{r}, t) = M_T(\vec{r}, 0) \cdot exp\left(i\gamma \int_0^t G(t) \cdot \vec{r} d\tau\right) \tag{2.15}$$

where $M_T(\vec{r}, t)$ is the transverse magnetisation in terms of positional vector $\vec{r}$ and time t. G is a time dependent gradient applied during time τ. The signal, S(t), induced in the coil is based on the magnetisation $M_T(\vec{r}, t)$ and can be found by integrating equation 2.15 over the entire volume

$$S(t) \propto M_T(t) \propto \iiint_R \rho(\vec{r}) \cdot exp\left(-i\gamma \int_0^t G(t) \cdot \vec{r} d\tau\right) d\vec{r} \tag{2.16}$$

where $\rho(\vec{r})$ is called the proton spin density operator and is proportional to the magnitude of $M_T(\vec{r})$ at location $\vec{r}$ after excitation. The MR signal at a given time t is given by the Fourier transform of the spin density function $\rho(\vec{r})$. Equation 2.16 gives the signal from the entire volume, and not slice by slice. By applying a 2D Fourier transform on the spin distribution, after a slice selective RF-pulse, the magnetisation distribution is given by:

$$M_T = \iint_{slice} \rho(\vec{r}) \cdot (-i\vec{k} \cdot \vec{r}) d\vec{r} \tag{2.17}$$

Equation 2.17 describes the relationship between the spin density of the imaged object and the acquired MR-signal under influence of field gradients. $\vec{k}$ is a vector containing information about the spatial frequencies of the image. In direction d, where d represents either the x, y or z-direction, it is given by

$$k_d = \gamma \int_0^t G_d(\tau) d\tau \tag{2.18}$$

where G_d is a time-dependent gradient in the d-direction. With a known gradient configuration, the spin density can be found by an inverse Fourier transform of the measured transverse magnetisation

$$\rho(x,y) = \frac{1}{2\pi} \int_{k_x} \int_{k_y} S(k_x k_y) exp(i(k_x x + k_y y)) dk_x dk_y \tag{2.19}$$

where $S(k_x k_y)$ is the signal intensity measured with known applied gradients. The protons phase-and frequency distribution of Larmour frequencies is given by $exp(i(k_x x + k_y y))$.

2.4.4 Phase-encoding gradient

An alternative to the slice selective gradient is a phase-encoding gradient, used for 3D-acquisition schemes [4]. Slice thickness of 2D-acquisition is limited by the available strength of the gradient and signal-noise-ratio considerations. In 3D-acquisition, the whole volume of interest is excited using a non-selective RF-pulse and a phase-encoding gradient applied in the slice direction [4]. The spin distribution is then given by

$$\rho(x,y,z) = \frac{1}{2\pi} \int_{k_x} \int_{k_y} \int_{k_z} M_T(k_x, k_y) exp(i(k_x x + k_y y + k_z z)) dk_x dk_y dk_z \tag{2.20}$$

with the slice thickness given by

$$\Delta z = \frac{2\pi}{\gamma G_{z\_max} T_z} \tag{2.21}$$

where G_{z_max} is the peak value of the phase encoding direction in the slice direction and T_z is the gradient duration.

2.4.5 Echo sequences

Inhomogeneities in the magnetic field causes a rapid signal loss due to a loss of coherent transverse magnetisation. This loss means that there is not sufficient time for T_1 and T_2 to relax completely, and a regeneration of the signal is needed. This can be done either by using a spin echo pulse sequence or a gradient echo pulse sequence. Spin echo pulse sequence use a 180°pulse to regenerate the signal and gradient echo pulse sequence uses gradients for the same purpose.

Spin echo pulse sequence

A 90° RF-signal pushes the net magnetisation vector into the transverse plane. The nuclei in the transverse plane induces a signal in the receiver coil, which rapidly decreases after the RF-pulse is removed due to T_2^* dephasing. The T_2^* dephasing causes too rapid relaxation and the measured signal is insufficient. This is where a 180°RF-pulse comes in and compensates. When the magnetic moments start dephasing after the first 90°RF-pulse, some moves faster "away from coherence" than others. After a given period of time, the 180°RF-pulse is applied which flips the magnetic moments the opposite way. This results in the protons precessing towards coherence, and when coherence is achieved a new signal is given signal.

A way to picture this is an analogue watch with one hand for hours, one for minutes and one for seconds. As illustrated by Figure 2.6A the hands move in different speeds away from the start time t_0, say 12 o'clock. If the watch suddenly flipped after a minute, and hands starts moving counter clockwise, the hands will catch up to each other after another minute. For the magnetic moments, this is where transverse magnetisation is in phase and maximum signal in the coil is regained. This signal is called spin echo and contains information of both T_1 and T_2. The T_2^* has been reduced because of the extra relaxation time given.

MRI is very susceptible to movements and by introducing a term called turbo factor one can reduce the image acquisition time. Conventional spin echo makes use of one 180° flip per TR, which means one row of k-space is filled. A way of shortening the acquisition time is to use multiple 180° rephasing pulses per TR. Every time the magnetic moments rephases an echo is produced, and a new row in k-space is filled. The number of phase encoding per TR is called the turbo factor. If the turbo factor equals 10, the total acquisition time is reduced to 1/10 of the original time [7]. A spin echo sequence with these attributes is called a Fast Spin Echo sequence (FSE).

Gradient echo pulse sequences

Gradient echo starts with an RF-pulse which flips the net magnetisation vector, but here the flip angle can be anything and is usually less than 90°. In this case the magnetic moments within the transverse component is rephased using gradients. To use the analogous clock again, instead of flipping the clock making the hands go counter clockwise, gradient causes the hands to change their speed. As illustrated by Figure 2.6B, when the gradient is changed and the arms switches velocity, and the arms that was initially slow catches up with the previously faster ones until they meet up back in synchronisation and gives a clear signal.

Gradients rephase faster than 180° pulses, and this shortens the needed TE which ultimately shortens the needed TR, and hence the scan time. A problem is that there is no compensation for magnetic field inhomogeneities and T_2^* effects are not eliminated. For T_1 weighted images, neither water nor fat should have time to fully recover full longitudinal magnetisation before the next RF-pulse is applied.

An example of a specific gradient echo sequence is the Spoiled gradient echo sequence (SPGR) and is a sequence where the transverse signal is demolished before each RF-pulse. By doing this only the longitudinal magnetisation reaches its equilibrium and the image is therefore T_1-weighted. This is achieved by choosing a very long repetition time, $TR >> T_2$, and a short echo time, $TE << T_1$. The signal intensity is given by

$$S = M_0 \frac{sin(\alpha)\left(1 - exp\left(\frac{-TR}{T_1}\right)\right)}{1 - exp\left(\frac{-TR}{T_1}\right)cos(\alpha)} exp\left(\frac{-TE}{T_2^*}\right) \tag{2.22}$$

By deriving Equation 2.22 in terms of α and set it equal to zero, the optimal flip angle α_e is found. α_e is known as the "Ernst angle" and equals:

$$\alpha_e = cos^{-1}\left(exp\left(\frac{-TR}{T_1}\right)\right) \tag{2.23}$$

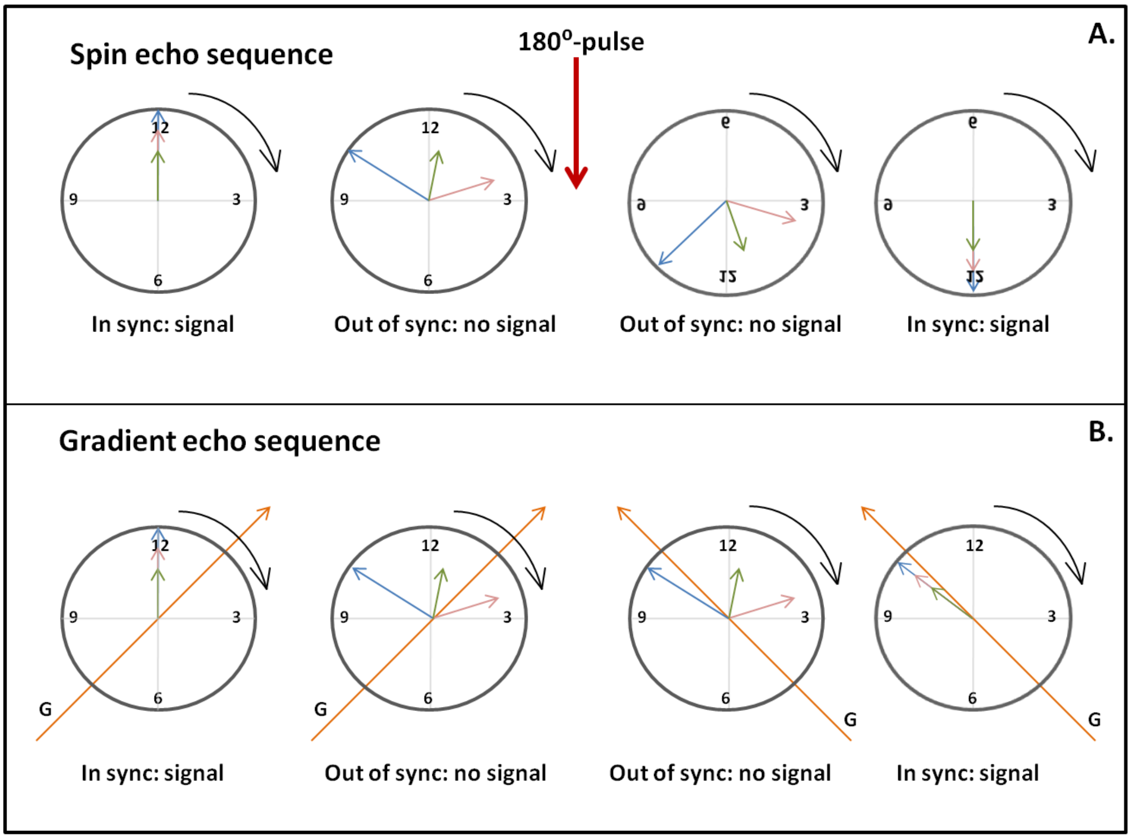

Figure 2.6: Simplified illustrations of Spin echo sequence (**A**) and Gradient echo sequence (**A**). Blue arrow shows seconds, red arrow shows minutes and green arrows shows hours in the watch analogy. The orange arrow (**G**) in **A** illustrates the gradient ($\vec{G}$).

2.4.6 Dynamic contrast enhanced magnetic resonance imaging (DCE-MRI)

Perfusion describes the regional blood flow in tissue and is defined as the volume of blood that flows into one gram of tissue [7]. Since less than 5% of tissue protons are intravascular, imaging blood volume in tissue is challenging. One way to measure perfusion is to increase signal intensities from perfusing spins by introducing an enhancement agent. When injected into the blood, these agent produce large magnetic moments in the capillary network which creates magnetic fields that extends into the adjacent tissue [7]. Perfusion is used a measure of the quality of vascular supply to the tissue.

Dynamic contrast enhanced magnetic resonance imaging (DCE-MRI) can be used to characterise the level of perfusion. It is particularly suited for cancer research, since tumours usually have a more rapid and higher uptake of contrast fluid than normal tissue [47].

Dynamic contrast enhanced imaging uses a fluid containing a contrast agent, usually para-magnetic tracers, to highlight certain parts of the image. These contrast agents shorten the T_1 or T_2/T_2^* relaxation times and can either enhance signal intensities for T_1-weighted images, or diminish signal intensities in T_2/T_2^* weighted images.

Contrast agent

A contrast agent is a paramagnetic ion metal with an unpaired electron in its outermost orbital shell, which makes it a magnetic dipole when in a magnetic field. The contrast agent spin is often up to 700 times larger in magnitude than that of a proton [4]. The heavy mass gives rise to large fluctuating magnetic fields that, when oscillating close to the Larmour frequency of the surrounding protons, greatly reduce the relaxation time of these protons.

The most commonly used agents are variants of the element gadolinium. Gadolinium (Gd^{3+}) is poisonous on its own, but the toxicity is reduced in combinations with ligands, such as Gd-DOTA (1,4,7,10-Tetraazacyclododecane-1,4,7,10-tetraacetic acid) [17]. Gadolinium is element number 64 in the periodic table and its relatively large mass and seven unpaired electrons makes it a good agent for T_1-based dynamic imaging [4].

In an experiment with mice, Weinman et al. [50] found that only 0.3% of the contrast agent was found in the body after seven days, the rest was removed in the excrement and urine. However, recent findings discovered that patients with lowered function of kidneys may experience serious complications when given variants of Gadolinium [34]. It has also been shown that Gadolinium accumulates in brain tissue. The consequences of this remains unclear, but there are concerns regarding the effects on patients [21].

Estimating concentration

Contrast agents diffuses into the ECM and the uptake of the agents can be decided through physiological parameters such as blood perfusion, permeability and extracellular space [4]. Tofts et al. [44] developed a pharmacokinetical model in 1999 that can be used to determine these different physiological parameters. The Tofts pharmacokinetic model needs an estimation of the concentration of contrast agent, C_t, at time t to estimate its physiological parameters.

The concentration of contrast agent can be estimated with sequences that are optimally sensitive to T_1 effects, and minimally sensitive to effects caused by T_2/T_2^*. This eliminates effects caused by transverse relaxation and signal saturation. The relaxation rate of T_1 due to contrast agents is described by

$$\Delta R_1(t) = R_1(t) - R_1^0 = C_t(t) \cdot r_1 \tag{2.24}$$

where $R_1^0 = 1/T_1^0$ and $R_1(t) = 1/T_1$ describes T_1-relaxation rates [4]. R_1^0 relates to the relaxation prior to the the contrast agents and $R_1(t)$ relates to the relaxation rate at time t after injection. $C_T(t)$ is the concentration of the contrast agent at time t, and r_1 is the relaxivity of the contrast agent. The relaxivity depends on the contrast agent and its surrounding environment. The change of relaxation rate in tissue is proportional to the concentration of contrast agents in the tissue. Phantoms with known concentrations of the contrast agent can be used to determine the relaxivity r_1 [3].

Measuring T_1-relaxation is a time consuming process, and temporal resolution is often sacrificed [4]. A way to avoid this is to use a heavily T_1-weighted gradient echo sequence, where $TR << T_1$ and $TE << T_2^*$.

The way signal intensity depends on contrast agents, tissue parameters and sequence parameters are rather complex. Hence, there are several steps on the way to proper DCE-MRI results. As Equation 2.24 shows, the concentration can be found by estimating the difference in relaxation rate of the tissue before and after the injection of contrast agent. The first step is to calculate the relaxation rate in the tumour without any contrast agent creating a R_1^0 map, sometimes referred to as a T_{10} map [19][44]. A T_1-weighted fast spin echo sequence (FSE) can be used to create the map. An FSE sequence, discussed in Section 2.4.5, reads multiple echoes per excitation and uses 180°-pulses for rephasing. Using the measured signal intensity, the R_1^0 map is estimated using

$$S = S_0(1 - exp(-TR \cdot R_1^0)) \tag{2.25}$$

where S_0 is a constant depending on the proton density and scanner gain. R_1^0 is the relaxation rate and TR is the repetition time. Using different TRs and Equation 2.25, one can determine R_1^0.

When the relaxation rate of the tissue, R_0^1, without contrast agent is estimated, a T_1 weighted SPGR 3D-sequence can be used to estimate R_1 [19]. A 3D sequence means that instead of exciting the object slice by slice, the entire object is excited. The slice selective gradient is replaced by a phase encoding gradient. The imaging time is longer than for slice selective gradients and its length increases proportionally to the number of phase encoding gradients used. The SPGR sequence, described in Section 2.4.5, needs a short echo time ($TE << T_2^*$), so that T_2^* effects can be neglected. The SPGRs short imaging sequences gives the proper time resolution in the images.

S_0 can be affected by the contrast agent and needs to be estimated for the SPGR sequence before the contrast fluid is injected. This is done by using the average signal intensities, S_{pre}, from the precontrast images in the T_1SPGR-sequence. Using Equation 2.22 and the R_0^1 estimated from Equation 2.25, S_0 is be estimated by

$$S_0 = S_{pre}\frac{1 - cos(\alpha) \cdot exp\left(TR \cdot R_1\right)}{sin(\alpha) \cdot \left(1 - exp\left(TR \cdot R_1\right)\right)} \tag{2.26}$$

where the $exp\left(\frac{-TE}{T_2^*}\right)$ term of Equation 2.22 is assumed to equal 1 due to $TE << T_2^*$.

With the calculated S_0, the relaxation rate after the injection, R_1, can be determined. The signal intensity from the SPGR sequence, after the injection of contrast agent, is given by Equation 2.22

$$S = S_0\frac{sin(\alpha)\left(1 - exp\left(TR \cdot R_1\right)\right)}{1 - cos(\alpha) \cdot exp\left(TR \cdot R_1\right)} \tag{2.27}$$

where α is the flip angle. Using the time dependent relaxation $R_1(t)$ in Equation 2.24, the concentration $C(t)$ is given by

$$C_t(t) = \frac{R_1(t) - R_1^0}{r_1} \tag{2.28}$$

Determining physiological parameters

Tofts et al. [44] developed a standardised pharmacological model to determine the kinetic factors from the DCE-MRI. This is a two compartment model with one compartment representing the blood plasma, and one compartment representing the extravascular extracellular space (EES) in the tumour tissue. The change of contrast agent levels in the EES is assumed to be caused by diffusion in and out of the plasma. Another assumption is that the contrast agent diffuses freely and homogeneous between the compartments.

The two main parameters of the Tofts pharmacokinetic model are the transfer constant K^{trans} and the fractional volume of EES per unit volume of tissue v_e. $K^{trans}[min^{-1}]$ describes the flow of contrast fluid between the blood plasma and the EES. Its interpretation is dependent on the balance between capillary permeability and blood flow in the tissue. Two ideal scenarios can be extracted from this. Low permeability and high levels of blood flow results in K^{trans} depending on the area of permeability of the vessel walls. Here, K^{trans} purely describes permeability.

Oppositely, high permeability and low levels of blood flow, results in K^{trans} depending on blood flow and the hematocrit. In this case, K^{trans} describes blood flow. The hematocrit is defined as the fractional volume of red blood cells in the total blood volume. In high-permeability cases K^{trans} is equal to the blood plasma flow per unit volume of tissue, or

$$K^{trans} = F\rho_t(1 - Hct) \tag{2.29}$$

where F is perfusion of blood per unit mass of tissue $[ml/(g \cdot min)]$, ρ_t is the density of tissue and Hct is the hematocrit. High K^{trans} value might imply that there is good supply of blood, but one can not distinguish between permeability and blood supply [39].

v_e measures interstitial volume fraction and lies between 0 and 1. Values greater than 1 is unphysiological and can suggest that it is an area of necrotic and/or fibrotic tissue [3]. v_e reflects how much space is available for the contrast agent to accumulate in.

The time dependent change in concentration of contrast agent in the tissue is given by

$$\frac{dC_t}{dt} = K^{trans}\left(C_p - \frac{C_t}{v_e}\right) \tag{2.30}$$

where C_p is the concentration of contrast agent in the blood plasma. The contrast agent is not injected until after some images is taken as a part of the T_1-weighted 3D-SPGR sequence. Hence, the initial conditions $t = \mathit{0}$ is set to just before injection. The concentration in the EES is assumed to be zero, $C_t(t = 0) = 0$, which gives the following solution to equation 2.30:

$$C_t(t) = K^{trans} \cdot \int_0^t C_p(\tau) \cdot exp\left(-\frac{K^{trans} \cdot (t - \tau)}{v_e}\right) d\tau \tag{2.31}$$

where $C_p(\tau)$ is the concentration in the arterial plasma at time τ, also known as the arterial input function (AIF). AIF can be difficult to determine because of insufficient spatial resolution or lack of arterial vessels in the image plane [39]. One can overcome this by measuring the distribution of contrast agent in arterial plasma using blood samples from athymic mice. Benjaminsen et al. [3] did just this, with gadolinium based contrast fluid (5.0 ml/kg), and found the following population based AIF by regression analysis:

$$C_p(t) = A \cdot exp(-B \cdot t) + C \cdot exp(-D \cdot t) \tag{2.32}$$

where $A = 2.6 \pm 0.21\ mM$, $B = 0.080 \pm 0.017\ s^{-1}$, $C = 1.2 \pm 0.11\ mM$ and $D = 0.0010 \pm 0.00020\ s^{-1}$. The first term of the equation describes the diffusion of contrast agent from blood vessels to tissue, and the second term describes the excretion of contrast agent to the kidneys. This model was shown to be a good, general estimate for genetically identical mice [3]. However, if this method is used in human patients, indvidual AIFs should be estimated each patient.

Egeland et al. [15] showed that tumours with high K^{trans} and v_e values had low levels of hypoxia, and tumours with low values of K^{trans} and v_e were highly hypoxic. This study also found K^{trans} to be more important for distinguishing between high and low fractions of hypoxia than v_e.

2.4.7 Diffusion weighted magnetic resonance imaging (DW-MRI)

As for molecules in most fluids, the molecules in the extracellular space move around freely and randomly due to their thermal energy [7]. The displacement of molecules due to this random motion is referred to as diffusion [1]. Diffusion is restricted by physical obstructions such as ligaments, membranes and macro-molecules, and molecules in the intracellular matrix [7]. Measuring diffusion can be used to locate diseased tissue.

Diffusion weighted magnetic resonance imaging (DW-MRI) makes use of the variation in movement, and measures diffusion via the Apparent Diffusion Coefficient (ADC). ADC gives the displacement of molecules across an area per second[7] and is a measure of water diffusion [48]. The effective displacement of water molecules, described by diffusion, is highly influenced by the cellular environment [23]. Cellular density, cell type and their organisation are examples of how water diffusion is influenced [23]. Collagen is shown to impede water diffusion and ADC should therefor be a good parameter to reflect collagen content. Hauge et al. [23] confirms this for collagen I content in models of uterine cervical cancer.

When using an echo sequence stationary nuclei, affected equally by the magnetic field $\vec{B}_{eff}$, maintain clear echo signals throughout the image acquisition. Freely moving nuclei, however, move in various directions and therefore experience different magnetic field strengths as they move through the gradient field. Since they are affected differently, giving them diverse Larmour frequencies, they do not reach coherence with their neighbouring protons. This diminishes the echo signals in voxels containing a lot of movement. By using different gradients the level of diffusion in different directions can be observed by the signal loss. Thus, DW-MRI measures the loss of signal due to protons in movement.

DW-MRI uses a diffusion sensitising bipolar gradient pair called a Stejskal-Tanner sequence that results in zero net effect of the gradients for stationary spins [4]. The sequence is described in Figure 2.7 with the first pulse inducing a phase shift equal to $\gamma \delta G \cdot r$, where γ is gyromagnetic ratio, δ is the diffusion gradient duration, G is the gradient and r is the position of the spin. Figure 2.7 also shows the diffusion time Δ. The diffusion time is the time from the first to the second gradient pulse. The second phase shift induce a negative phase shift $-\gamma \delta G \cdot r'$. r' describes the new position of the non-stationary spins.

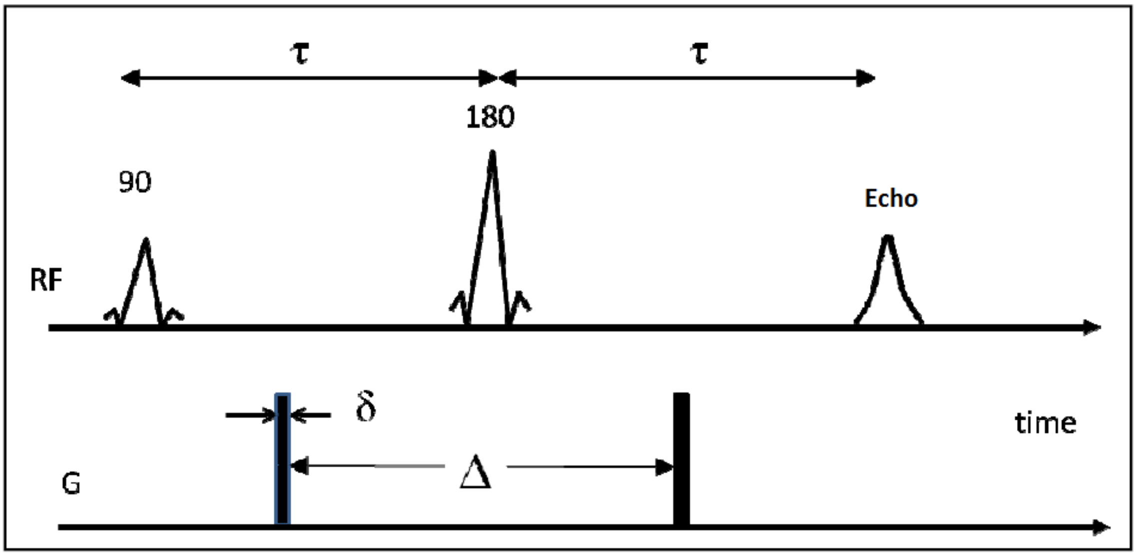

Figure 2.7: Figure illustrating the Stejskal-Tanner sequence. τ shows the space between RF-pulses ($TE = 2 * \tau$), G is the gradient, δ is the length of the gradient pulse and Δ is the duration between the pulses. The figure is borrowed with approval from [4]

The signal intensity *S(b)* for DW-MRI as a result of the magnetisation is described by the equation

$$S(b) = S(0)exp(-\gamma^2 G^2 \delta^2 \Delta D) = S(0)exp(-b \cdot D) \tag{2.33}$$

where D is the diffusivity and $b = \gamma^2 G^2 \delta^2 \Delta$ is referred to as the b-value. The b-value determines the amount of diffusion weighting in a sequence and has the unit $[s/m^2]$. A high b-factor gives a high diffusion weighting and the the MR-signal decreases mono-exponentially when b and D increases [4].

Instead of diffusivity D the Apparent Diffusion Coefficient (ADC) is commonly used. This is due to various forms of diffusion in the tissue with both intra- and extracellular diffusion. Additionally, blood perfusion is in some cases be interpreted as diffusion. The different forms of diffusion can be distinguished from each other by using various b-values, but may to some degree still influence the imaging. ADC can be referred to as the observable diffusivity and describes the diffusion length. High levels of ADC describes a long diffusion length with few barriers, which can for instance be a measure of the cell density [39].

Diffusion weighted images also contain T_2 weighting, and the relative signal when including T_2-effects is given by:

$$S(b, T_2) = S(0, T_2)exp(-b \cdot D)exp\left(\frac{TE}{T_2}\right) = S(0, T_2)exp\left[-\left(b \cdot D + \frac{TE}{T_2}\right)\right] \tag{2.34}$$

where T_2 is the T_2-signal and TE is the echo time. Equation 2.34 show that high diffusivity combined with long T_2 values may appear with normal or increased intensity, since the reduction in signal intensity due to high diffusivity may be counteracted by the long T_2 relaxation times. This can be avoided by calculating the actual diffusion, independent of T_2 effects [4].

The diffusivity D is replaced by the observable diffusivity ADC. ADC is estimated using a least square fit of the natural logarithm on varying signal intensities $(S(b, T_2))$ relative to the signal intensity of b = 0 $(S(b = 0))$. For this, at least two b-values is needed. The least square fit is based on

$$-\,ln\left(\frac{S(b)}{S(b=0)}\right) = b \cdot ADC + c \tag{2.35}$$

where c is a constant of fit, and ADC is given by the slope of the linear fit [19]. In the ADC map, voxels with high diffusivity will appear bright.

Chapter 3

Methods

3.1 Tumour models

This study investigates the effect of Losartan on cancer cell lines CK-160 and Capan-2. The xenograft CK-160 is a squamous cell carcinoma derived from a pelvic lymph node metastasis of a patient with a well-differentiated (histological grade I) keratinizing primary tumour [16]. The primary tumour responded well to radiation therapy, but was highly metastatic. The patient had developed pathological pelvic lymph nodes at presentation, and distant lymph node metastasis were discovered at the 1-year control [16]. The tumour model shows high levels of hypoxia, necrosis and collagen content [16][25].

Capan-2 is a panctratic ductal adenocarcinoma derived from a 56 year old male [11]. The primary tumour was located at the head of the pancreas and infiltrated a part of the small intestine on the side of the pancreatic duct. The patient underwent several surgeries and postoperative chemotherapy [11]. The tumour was well differentiated and had no metastasis [11]. It also shows clear signs of collagen I and hypoxia [48][49].

CK-160 and Capan-2 cancer cells were obtained from a frozen stock at the Norwegian Radium Hospital, and cultured in RPMI-1640 medium (25 mM HEPES and L-glutamine) supplemented with 13% bovine calf serum, 250 mg/l penicillin and 50 mg/l strepomycin. The cells were dissolved in 10 μ l Hanks balanced salt solution (HBSS), and injected intramuscularly into the gastrocnemius of the left hind leg of Balb/c *nu/nu* mice. The number of cells was approximately 5×10^5 cells for the CK-160 cell line and 3×10^6 for Capan-2.

3.2 General animal welfare

This study used adult female athymic Balb/c *nu/nu* mice, bred in the Animal Department at the Norwegian Radium Hospital. The mice were kept in a designated room with a temperature of $22.5 \pm 1\ °C$, a relative humidity of $62\% \pm 5\%$. The light in the room followed a circadian rhythm with 12 hours light (70 lux) and 12 hours dark (1 lux). Sterile food and water were fed ad libitum. The diet consisted of *Rat and Mouse No.3 Breeding pellets* delivered by Special Diets Service (SDS, Essex, UK) and were sterilised by irradiation before use as recommended by SDS Info-Sheet 050523 [40]. The water was acidified to pH 3 to avoid bacterial growth. Eurostandard type III cages (macrolone) were used and changed twice a week. The bedding consisted of Aspen wood (*Populus Tremula*) from Tapvei (Harjumaa, Estonia). The cage was also provided with enrichment such as paper and houses or tunnels.

Humane endpoints

The wellbeing of the animals was a priority. To prevent unnecessary suffering, the animals were inspected once a day. A mouse would be euthanized if it lost too much weight, showed signs of abnormal behaviour, signs of pain and distress, or a worsening of the general health. Euthanasia was achieved through cervical dislocation, and the mouse was anaesthetised during euthanization. Examples of behavioural and physical signs are unsocial and passive behaviour, closing of eyes, ears fixed and hanging, or an arched back. If a mouse turns sick, it is often shown by a combination of these signs.

There were no indications that Losartan should affect the health of the mice in a negative manner, so the human endpoints were established as a precaution before the study started. The endpoints were only relevant for a few mice. There was no difference in the number of mice that were euthanized due to sickness between the Losartan treated and non-treated groups. Half of the euthanized mice were euthanized before the treatment schedule started.

The main reason mice were excluded from the study was not due to sickness, but due to insufficient tumour growth and tumour cells being rejected by the mouse.

3.3 Treatment

The following procedure was used for the CK-160 and the Capan-2 cell lines, both containing groups treated with Losartan (Cozaar, Wilmington, Delaware, USA). The mice were divided into cages of 10 mice, where the mice of the cage was treated with either Losartan (Losartan group) or control (vehicle group).

One week after the injection of tumour cells, treatment with Losartan started and lasted for 3-5 weeks until tumours grew to about 400 mm^3. Losartan dose per treatment was 30 mg/kg mixed with a phosphate-buffered saline (PBS) to a concentration of 2.5 mg/ml. The injections were given intraperitoneally (i.p.), into the abdominal cavity. An equivalent volume of pure PBS were given to the vehicle group. Every mouse was weighed before each injection of Losartan or PBS to determine the correct volume. The weight was also logged, since a rapid gain or loss of weight was a good indicator of mouse health.

The mice were treated once a day from Monday to Friday, and received no treatment during the weekends. Since the pharmacology of a substance can change throughout the day, due to metabolic variation following the circadian rhythm, the daily treatment was given around noon each day [18].

Vascular density and blood perfusion is dependent on tumour size, so the tumours were imaged and analysed at the same volume [15]. The tumour size was judged by caliper measurement to get an approximation of the size. There was some uncertainty using a caliper, and the volume was therefore confirmed by an estimation from the images of a T_2-weighted FSE MR-sequence. If the tumour was too small, the mouse continued the treatment schedule and was imaged once more after several days.

3.4 Magnetic resonance imaging

3.4.1 Preparations and procedure

Anaesthesia was used when injecting the tumour cells, carrying out the MRI procedure and before euthanizing the mice. The inhalation anaesthesia Sevofluran (Baxter, Illinois, USA) was used in combination with O_2 [19]. Sevofluran is a halogenized inhalation anaesthetic that gives a painless sleep and causing the muscles to relax. It can, however, cause some irritation to the mucous membranes. The use of the inhalation anaesthesia ensures that the mouse rapidly falls asleep and gains consciousness quickly after the anaesthesia is removed.

Each mouse was placed in a small chamber containing airflow of 1 l/min of O_2, 2 l/min of N_2O and 5% Sevofluran until they fell asleep [39]. Because of its lipid solubility nitrous oxide, N_2O, transfers rapidly through the alveoli and increases the concentration and driving pressure of the anaesthetic agents [6]. The rapid uptake of N_2O improves the ventilation [6]. The eyes were lubricated with eye balm to prevent the cornea from drying out.

For the MRI procedure the mouse was moved to a gas mask for insertion of the cannula for the contrast agent. The contrast fluid was a mixture consisting of 0.5 M gadolinium mixed with 0.9% NaCl so that the concentration of the contrast agent was 0.06 M. The desired amount of contrast agent was 5.0 μl/kg and the mouse was therefore weighed to get the correct injection. When placing the venous catheter, the mouse was placed on a heated mat to prevent hypothermia and to expand the veins of the tail to make it easier to place the cannula properly. This is a laborious process, and it was important to avoid puncturing the opposing wall of the vein. If this is not done correctly the tail will be damaged when injecting the contrast fluid, and the images will be of no use. The cannula was fixated with medical tape and injected with heparinized saltwater to avoid coagulation.

After connecting the cannula to a syringe, the mouse was moved to the bed of the MRI. The syringe was connected to an extension tube that made it possible to inject the fluid while the mouse was inside the MRI. The mouse and cannula were fixated using tape and the volume coil was placed around the main body of the mouse. The syringe was connected to an automated infusion pump (Harvard Apparatus, Holliston, MA, USA), with the injection rate set to 0.037 ml/s.

During the MR-imaging the temperature and breathing frequency of the mouse was monitored. A hose blowing warm air of 37 °C was located at the inferior end the bed, and the temperature was measured using a rectal probe (Small Animal Instruments, New York, USA). The anaesthesia was set to a flow of 0.5 l/min and about 4% Sevofluran [19], but regulated so the breathing frequency stayed between 50 and 100 inhalations per minute. MR images are very sensitive to movement, and anaesthesia was therefore essential for collecting usable images and to avoid unnecessary discomfort for the mouse.

After the MRI was finished, the mouse was earmarked and monitored while waking up, before placing it back in the cage with the others. It is important that the mouse fully awake before joining the others, to avoid the other mice biting the sleeping mouse.

3.4.2 MR protocols

For the magnetic resonance imaging, a Bruker Biospec 7.05 T bore magnet was used with a mouse quadrature volume coil (Bruker Biospin, Ettlingen, Germany). The mouse was placed inside the volume coil so that the tumour was located in the magnetic isocenter. The volume coil was tuned with the mouse inside to achieve a homogeneous magnetic field.

A summary of the five step imaging protocol is presented in Table 3.1. The protocol was previously developed by the Research group (Group of Radiation Biology and Tumour Physiology) at the Department of Radiation Biology at the Norwegian Radium Hospital (Oslo University Hospital). To make sure the tumour was placed in the isocenter, the protocol started with a localisation sequence [39]. This is a T_1 weighted SPGR sequence with three sections, one axial, one sagittal and one coronal. An anatomical T_2 weighted FSE sequence, consisting of 14 axial sections, was done to make sure the mid section covered the middle of the tumour and that the tumour was sufficiently covered in all imaging sequences. The thickness of each slice was 0.7 mm with a 0.3 mm gap between each slice.

Thereafter, a DW-MRI sequence was conducted with a diffusion-weighted single-shot fast spin echo pulse sequence (FSE) with the same slice thickness and gap as the previous step [39]. Four diffusion encoding constants were chosen, where b equalled 200, 400, 700 and 1000 s/mm^2. The sequence used a constant diffusion gradient duration of 7 ms (δ) and diffusion separation time of 14 ms (Δ). Three orthogonal diffusion sensitisation gradients with the physical gradient combinations [1 0 0],[0 1 0],[0 0 1] were used. Three sensitisation gradients were used since DW-MRI are easily affected by movement, and diffusion is measured in three directions to compensate for this. An average of the signal from the directions with sufficient signal-to-noise ratio was used to represent the degree of diffusion in the voxel. The strength of the gradient G varied with different b-values. To further prevent noise, the voxel size was quadrupled in the DW-MRI-sequence.

The fourth step consisted of a mapping sequence (R_1^0-map). The precontrast T_1 values, used to decide the R_1^0-map of the tumour, was found by an FSE pulse sequence with varying repetition time (TR = 200, 400, 800, 1500 and 5000 ms). The 0.7 mm slice thickness and 0.3 mm gap was still applied. In the fifth and final step, 65 T_1 3D-SPGR images were taken [39]. Six of the images were taken before the injection of contrast fluid and 59 images after. Using 10 slices with resolution of 128 × 128 pixels and a FOV of 30 × 30 × 10 mm^3 gave a spatial resolution of 0.234 × 0.234 × 1 mm^3. The TE had to be as low as possible, and was chosen to be 2.07 ms. The 3D-SPGR sequence had a time resolution of 14,8 s and a total imaging time of 15 minutes and 15 seconds. The DCE-MRI sequence was the last sequence to avoid the contrast agent influencing the other imaging sequences.

Sequence	**TR** [ms]	**TE** [ms]	**Flip angle** [°]	**Imaging time**	**Voxel size** [mm^3]	**Field of view (FOV)**
Localisation (T_1 SPGR)	100	3	30	12.8 s	0.156 × 0.156 × 1	40 × 40 mm^2
(T_2 FSE)	2500	35	90 and 180	1 min 20 s	0.234 × 0.234 × 0.7	30 × 30 mm^2
DW-MRI (T_2 FSE)	1100	26	90 and 180	13 min 12 s	0.469 × 0.469 × 0.7	30 × 30 mm^2
Mapping (T_1 FSE)	200-5000	8.5	90 and 180	8 min 21 s	0.234 × 0.234 × 0.7	30 × 30 mm^2
DCE-MRI (T_1 3D-SPGR)	10	2.07	20	15 min 15 s	0.234 × 0.234 × 1	30 × 30 × 10 mm^3

Table 3.1: Summary of MRI protocol.

3.5 Magnetic resonance imaging analysis

The MR-images were imported in *DICOM*-format (Digital Imaging and Communication in Medicine) and further analysed using Matlab R2013b (Mathworks, Natick, MA, USA). Software used for further analysis was developed by Dr. Jon-Vidar Gaustad at the Group of Radiation Biology and Tumour Physiology, Department of

Radiation Biology, Norwegian Radium Hospital. The software analyses the images voxel by voxel. Using the T_2 FSE images a Region of Interest (ROI) was drawn at the periphery of the tumour in each slice, and used to calculate the tumour volume. The ROIs were drawn manually using Matlab and used for both the DCE-MRI and the DW-MR images, making sure they were analysed based on the same areas of the tumour.

3.5.1 Estimating K^{trans} and v_e

To control that the uptake of contrast fluid was sufficient, the uptake in the tissue of a muscle (outside the tumour) was measured. If the uptake of contrast fluid was not sufficient, the images of the DCE-MRI sequence were not included in the study.

K^{trans} and v_e were determined through a curve fitting of Equation 2.31 in Toft's model. For this, the R_1^0-map, S_0 and the change of relaxation rate ΔR_1 were needed. From the T_1-FSE mapping sequence, the R_1^0-map was made voxel by voxel through a curve fitting of Equation 2.25. The curve fit was based on six different repetition times between 200-5000 ms and a logistic regression of the resulting curve. Next, the first six images of the T_1 3D-SPGR sequence, before contrast fluid injection, was used to calculate S_0 via Equation 2.26. $R_1(t)$ was found for each time t of the imaging sequence using the determined S_0 and solving Equation 2.27 numerically. Equation 2.28 was then used to calculate $C_t(t)$.

The arterial input function, $C_p(t)$, is known in advance and is given by Equation 2.32. $C_p(t)$ was used with $C_t(t)$ to find the parameters K^{trans} and v_e. Equation 2.32 and the coefficients A, B, C and D estimated by Benjaminsen et al. [3], were assumed to be applicable for all mice. The time development of $C_p(t)$ and $C_t(t)$ were used to estimate K^{trans} and v_e for all voxels using Equation 2.31.

Figure 3.1 visualise the measured contrast of a individual voxel. The abscissa shows the time in seconds, and the ordinate shows the concentration $C_t(t)$. The points in the plot are the concentrations at given time, and a curve adaptation to these points gives the parameters K^{trans} and v_e.

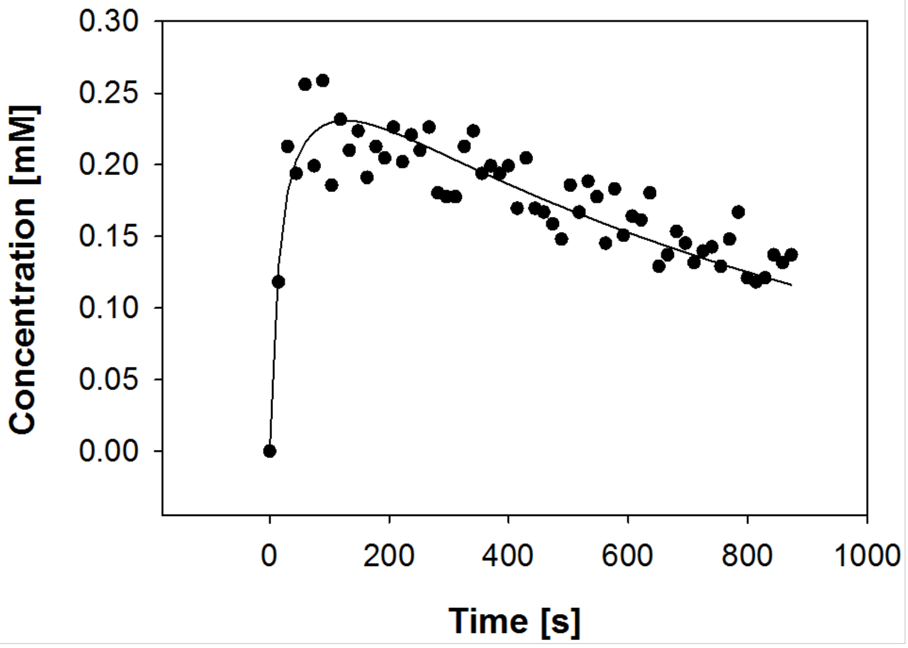

Figure 3.1: The figure shows an example of how K^{trans} and v_e is estimated in a voxel using the concentration versus time data. The black points show the measured concentration for a point in time. The black line is the curve fit of these points. The physiological parameters K^{trans} and v_e were estimated based on this curve.

Values of K^{trans} and v_e for each voxel were stored and used to estimate median values for sections and tumours. These were also used to calculate histograms, used for investigating the distribution of values in the tumours. Since v_e is a measure of fractional volume, values above 1 are not physiological [19], and these voxels were therefore removed. New median values were calculated for K^{trans} and v_e. K^{trans} and v_e vectors were used to create histograms. Additionally, matrices for K^{trans} and v_e were extracted and imported to Sigmaplot Version 14.0 (Systat Software, San Jose, CA, USA) to create K^{trans} and v_e images for visualisation. These images consisted of K^{trans} or v_e values within the ROI, with the values outside of the ROI set to zero. The fraction of voxels removed could be an indication of the level of necrotic and/or fibrotic tissue in the tumour, and was therefore also saved [49].

3.5.2 Estimating the Apparent Diffusion Coefficient

The same ROI drawn in the analysis of K^{trans} and v_e was used for estimating ADC. Since diffusion weighted imaging is susceptible to noise, the average signal intensities of the three directions in each voxel were used for further analysis. For every voxel the measured signal intensity of each b-value in each direction was averaged. The average signal, relative to the average signal of $b = 0$, was used to estimate ADC using the linear least square fit algorithm on Equation 2.35. Equation 2.35 used the natural logarithm of the estimated signal intensity, $(S(b)/S(b = 0))$, for different b-values (200, 400, 700 and 1000 s/mm^2). ADC is given by the as the slope of the linear fit.

The ADC values and corresponding R^2 was saved for each slice. The median ADC value of the tumour was used to represent the tumour. For diffusion weighted images the median R^2 values were used to prevent using images with too much noise. Tumours with a R^2 value below 0.9 were excluded from the overall analysis. As for DCE-MRI, matrices with ADC values was extracted for each slice and imported to Sigmaplot for visualisation.

3.6 Histology

After completing the MRI examination the mouse was euthanized. This was done the same day, or no later than within the next day. The tumour was then extracted rapidly after euthanization and stored in a small metal container. The metal container was placed in an isotherm bucket with liquid nitrogen for transportation, and stored in a freezer at -80 °C.

In addition to parameters derived from the MRI sequences, the levels of hypoxia, collagen and necrosis were measured. To measure hypoxia levels, 30 mg/kg of the marker Pimonidazole was injected i.p. three to four hours before extracting the tumours. Pimonidazole is an hypoxic marker that binds irreversibly to macromolecules in hypoxic cells and only metabolise under hypoxic conditions [22]. Pimonidazole in hypoxic areas is then detectable in biopsies and immunohistochemistry.

Tumours were sectioned and sent to a pathologist for staining. Histological sections were prepared by standard procedures and stained with collagen I anitbody, hematoxylin and eosin (HE), and a pimonidazole antibody. HE highlights cell nuclei and cytoplasm and is used to differentiate between viable and necrotic tissue. The images were used to distinguish viable from necrotic tissue. An anti-collagen I rabbit polyclonal antibody (Abcam, Cambridge, UK) was used as primary antibody for the sections used to estimate the fraction of collagen I in tumours.

The stained slices were scanned using a Hamamatsu Nanozoomer XR (Hamamatsu City, Shizuoka, Japan). Images were stored as NDPI files and were converted to TIF using software developed by Cristophe Deroules et al. [12] for further analysis. ImageJ (NIH, Bethesda, Maryland, US) was used to measure the fraction of hypoxia, collagen and necrosis. Only one section, derived from the middle of the tumour was used when estimating fraction of hypoxia, necrosis, collagen I and connective tissue. The mid section was assumed to reflect the overall levels in the tumour.

The estimation of hypoxic, necrotic and collagen I fraction was done manually for both Capan-2 and CK-160 tumours. This was due to a lack of accurate automatic methods, for instance region growing or colour thresholding. The overall intensity varied between and within the images and finding a global threshold was therefore challenging. ImageJ was used for all of the histological analysis.

The immunohistochemistry staining was not sufficient for all tumours in the CK-160 model, and the number of histological samples analysed differed from the number of mice completing the MR imaging.

3.6.1 Hypoxia

When estimating the hypoxic fraction the images stained with pimonidazole were used. For CK-160, a region of interest (ROI) was drawn around the tumour, the necrotic areas and the hypoxic areas. Hypoxic fraction was calculated as the sum of hypoxic areas divided by the non-necrotic area. The necrotic fraction, calculated by dividing the sum of necrotic areas by the tumour area, was also collected and compared between the treated and untreated groups.

For Capan-2 tumours, on the other hand, clear regions of interest were harder to draw due to the high mix of fibre and hypoxia in small areas. Hence, the ROI method was exchanged to counting points of interest. To measure the hypoxic fraction, the number of vertices containing hypoxia was counted in the area of interest and divided by the total number of vertices in the tumour section.

3.6.2 Collagen

Similar to the hypoxic fraction calculation for Capan-2, estimating collagen fraction was done by counting points of interest. Necrotic fraction was calculated for the these images as well, and compared to the necrotic fraction estimated from the pimonidazole antibody stained histological images, to see if the regions had been drawn correctly.

There were issues with the batch of collagen I antibody used for staining Capan-2 sections, and immunohistochemistry images for collagen were therefore not collected. As a substitute, the same images used to calculate hypoxia were used in combination with the HE images as a rough estimate for connective tissue. Without staining one cannot distinguish collagen form other types of connective tissue, but one could distinguish connective tissue from other tissues. This fraction was also estimated by counting points of interest.

3.7 Statistical analysis

The Shapiro-Wilk test was used to test for normality and the Brown-Forsythe test was used to test equal variance. Under the assumption of equal variance, the Student's t-test was used to test statistical significance. Welch's test was used when equal variance could not be assumed. Probability values of $P < 0.05$, determined from the two-tailed t-test, were considered significant. The statistical analysis was performed using SigmaPlot statistical software Version 14.0 (Systat Software, San Jose, CA, USA).

Chapter 4

Results

4.1 Tumour information

It is common in experimental tumours that the tumour parenchyma outgrows the vascular network. Vascular density and blood perfusion therefore decrease with increasing tumour size [15]. Large tumours often have lower perfusion and more hypoxia than smaller ones. It was therefore important that the size of the tumours in the treatment group and control group were similar. The tumours grew until they reached approximately 400 mm^3 before they underwent MR imaging and extraction, as illustrated by Figure 4.1A. As seen in Figure 4.1A the size of tumours did not differ between the two groups when (P >0.05).

Non-differentiated tumours have been shown to grow slower for some tumour models, possibly due to collagen synthesis restricting tumour growth [48]. The MR parameter ADC, which can be used to reflect collagen I content, has been shown to decrease with increasing tumour growth rate [23][48]. Losartan treatment did not affect tumour growth rate for Capan-2 (P >0.05) or CK-160 (P >0.05) tumours as shown by Figure 4.1B. This implies that Losartan did not affect the degree of differentiation in the tumour models. Also, ARBs have been shown to cause a delay in tumour growth [9], but this was not the case for either CK-160 or Capan-2 tumours.

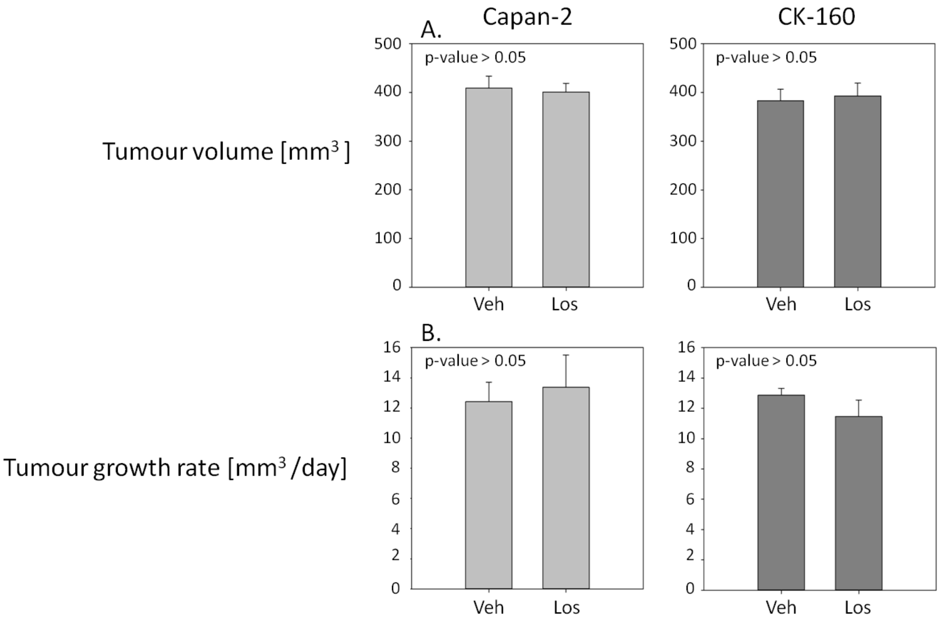

Figure 4.1: Tumour volume (**A**) and tumour growth rate (**B**) of untreated (Veh) and Losartan-treated (Los) tumours. Bars show mean of 5 Capan-2 Veh, 9 Capan-2 Los, 9 CK-160 Veh, and 10 CK-160 Los. Error bars show standard error.

4.2 Hypoxic fraction

Immunohistochemistry images of tumour sections showed that hypoxic areas were scattered around the tumour, as illustrated by Figure 4.2A-B. The central areas of the Capan-2 tumours contained the majority of the hypoxic tissue, and the periphery of the tumours appeared more oxygenated. The periphery of CK-160 tumours also showed less hypoxic tissue than the central regions, although this difference was smaller for CK-160 tumours than for Capan-2 tumours. CK-160 tumours also showed necrotic regions, and Losartan-treated tumours showed fewer and smaller necrotic regions than the untreated tumours.

Hypoxic fractions varied within the two tumour models. For CK-160 tumours, the hypoxic fraction varied from 8% and up to 55%, with an average of 26 %. The differences within the Losartan-treated group and vehicle group were larger than between the two groups. This was not the case for Capan-2 tumours which differed in hypoxic fraction between Losartan-treated and non-treated tumours. Losartan-treated tumours varied from 10% to 35%, and had an average value of 26%. The lowest hypoxic fraction value of the Vehicle tumours was almost as high as the average fraction value for Losartan-treated. Vehicle tumours in Capan-2 varied from

23% and up to 41%, with a mean value of 34%. For untreated tumours, Capan-2 contained higher levels of hypoxia while CK-160 tumours showed a wider range of hypoxic fraction values.

This is summarised in Figure 4.2C and D. Capan-2 tumours showed a tendency towards lower hypoxic fractions in Losartan-treated tumours as displayed in Figure 4.2C. This reduction was not significant (**P >0.05** (0.09)), but reflected the expected response to Losartan treatment. CK-160 tumours on the other hand, did not show any reduction in hypoxic fraction as shown in Figure 4.2D. There was, however, a significant reduction (**P = 0.03**) in the fraction of necrotic tissue in tumours treated with Losartan.

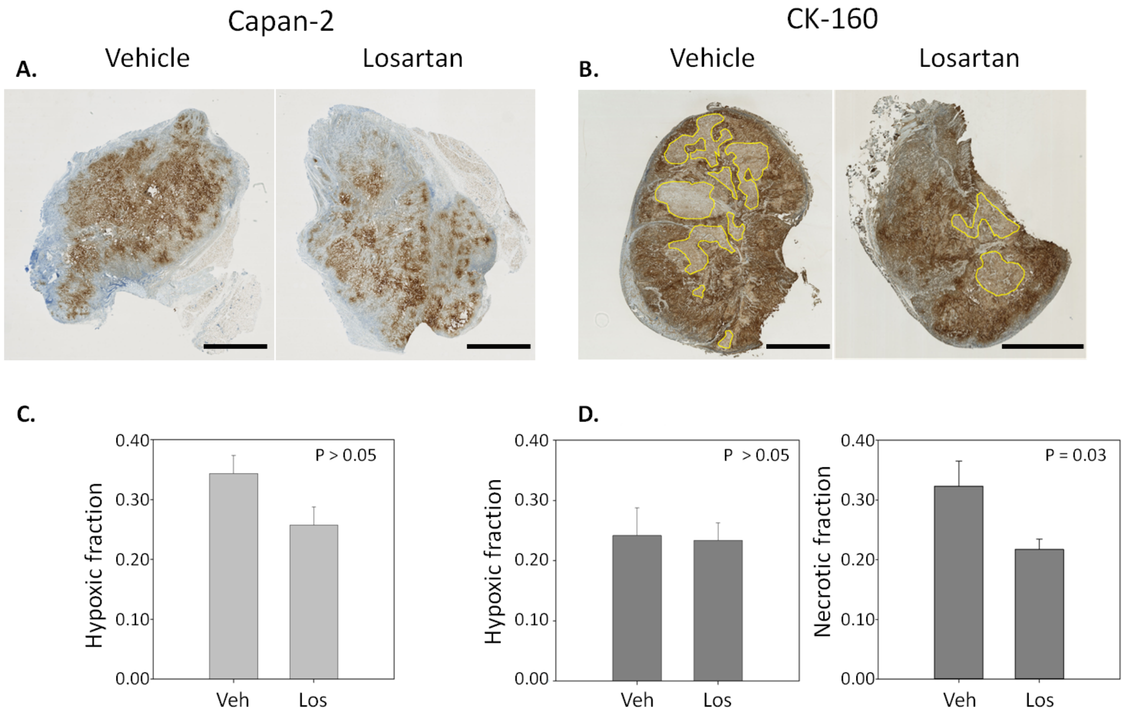

Figure 4.2: Histological samples of Capan-2 tumours (**A**) and CK-160 tumours (**B**) showing hypoxic areas in brown, together with hypoxic fraction for untreated (Veh) and Losartan-treated (Los) Capan-2 tumours (**C**) and CK-160 tumours (**D**). The areas marked yellow in **B** show necrotic tissue. Necrotic tissue fraction for untreated and Losartan-treated CK-160 tumours are shown in **D**. Bars show mean of 5 Capan-2 Veh, 9 Capan-2 Los, 8 CK-160 Veh, and 8 CK-160 Los. Error bars show standard error. Scale bar 2.5 mm.

Capan-2 tumours, in Figure 4.2C, contained borderline significant differences between Losartan-treated and non-treated tumours for mean hypoxic fraction values. An alternative method to evaluate the data is by using cumulative plots. Here, the relative frequency of hypoxic fraction values in Losartan-treated and non-treated tumours are plotted. There was a significant difference in displacement of hypoxic fraction values in Capan-2 tumours ($P = \mathbf{0.0011}$), shown in Figure 4.3A. The plot shows that Losartan treated tumours were displaced towards lower hypoxic fraction values, implying a significant reduction in hypoxia for Capan-2 tumours treated with Losartan.

The cumulative plot of CK-160 tumours in Figure 4.3B corresponded with previous results (Figure 4.2D) and shows that CK-160 tumours had no significant difference in displacement of hypoxic fraction values ($P > \mathbf{0.05}$).

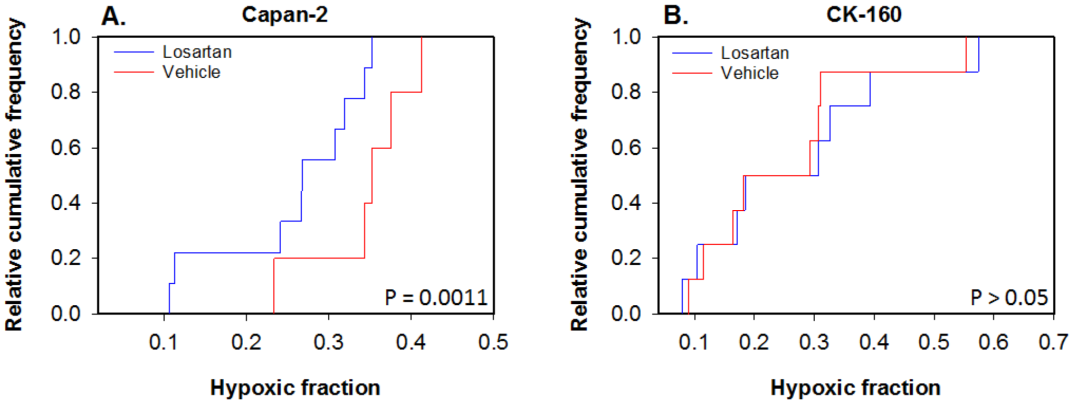

Figure 4.3: The cumulative plot hypoxic fraction in Capan-2 (**A**) and CK-160 (**B**) tumours are shown. Capan-2 tumours show a significant displacement towards lower hypoxic fraction values for Losartan-treated tumours ($P = \mathbf{0.0011}$). CK-160 tumours show no significant displacement ($P > \mathbf{0.05}$).

4.3 DCE-MRI

For each voxel in the DCE-MRI, the K^{trans} and v_e values were estimated using Equation 2.31 from Toft's model. This is illustrated in Figure 4.4 which shows the measured concentration, after the injection of contrast fluid, versus time for three individual voxels in Capan-2 tumours (A) and CK-160 tumours (B).

Figure 4.4A-B shows that voxels with high uptake of contrast agent were easily separable from voxels with low uptake. The signal-to-noise ratio was high enough that well defined pharmacokinetic fits were produced for the voxels in both tumour models. The voxels displayed in the plot are marked with white arrows in Figure 4.4C for Capan-2 tumours and D for CK-160 tumours.

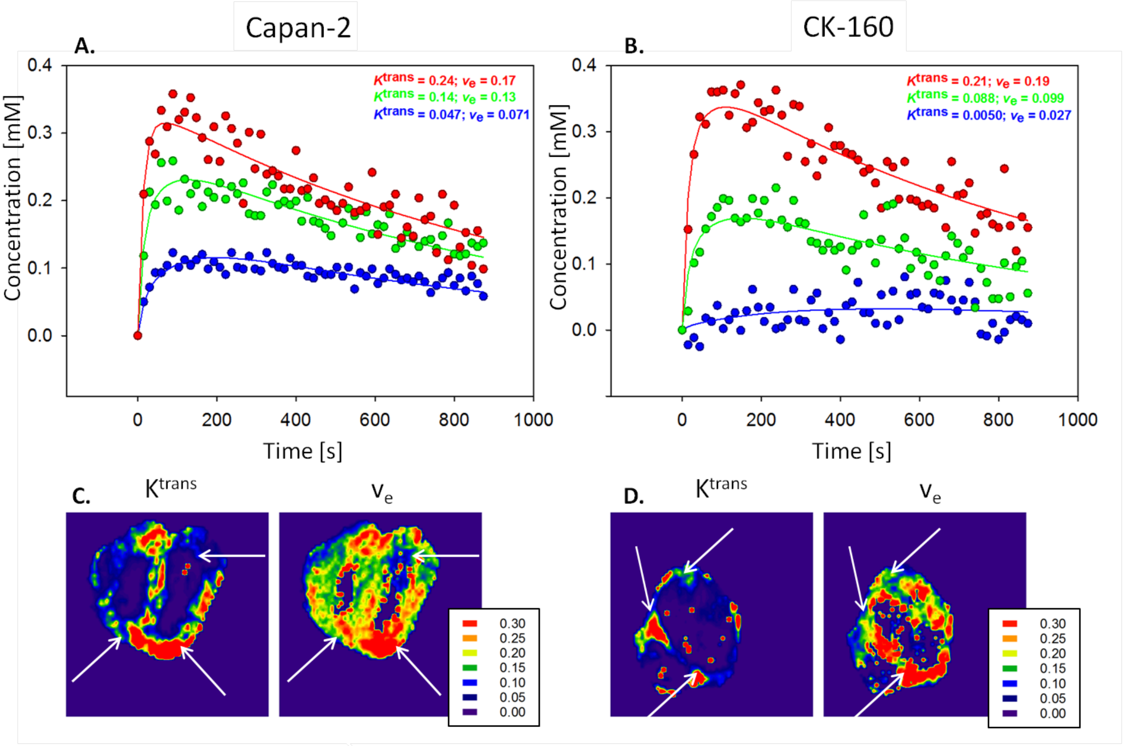

Figure 4.4: Estimation of K^{trans} and v_e values for three voxels using DCE-MRI and the Tofts pharmacokinetic model for a Capan-2 tumour (**A**) and a CK-160 tumour (**B**). Curve adaptation was based on the measured concentration [mM] after the injection of contrast fluid versus time [s]. The voxels represented as curves in **A** and **B** are marked with white arrows in **C** and **D**. **C** and **D** show K^{trans} (left) and v_e (right) images for Capan-2 tumours and CK-160 tumours, respectively. Values for K^{trans} $[min^{-1}]$ and v_e [fraction] are shown by colour scale in the legend.

K^{trans} and v_e images from representative Losartan-treated and non-treated tumours are displayed in Figure 4.5. Column A show that for both Capan-2 and CK-160, the high K^{trans} values were mainly located in the periphery of the tumour, while low values were located centrally. This is reflected by Figure 4.2A-B, showing a higher fraction of hypoxic tissue located in central areas of the tumours. Higher K^{trans} values indicate more perfusion, which corresponds well with higher oxygenation in these areas, as indicated by the histological images of Figure 4.2.

Corresponding K^{trans} histograms are shown in column B of Figure 4.5. Before calculating the distribution of values for the histograms, the voxels containing v_e

values larger than 1 were removed. The histograms of the Losartan-treated Capan-2 tumours shows a higher fraction of low K^{trans} values than the non-treated tumour. This is reflected by a lower mean K^{trans} value, marked with a red line in the histograms. The two bottom rows of Figure 4.5 show tumours of CK-160. The K^{trans} histograms show no substantial difference between untreated and Losartan-treated tumours.

For both tumour models, column C shows that v_e values were more scattered, with high high and low values in both central and peripheral areas. This illustrates that a higher fraction of interstitial volume, given by high v_e values, does not necessarily correspond with the degree of hypoxia. Voxels containing unphysiological v_e values ($v_e > 1$), were assigned the value zero and appear dark blue in v_e images in column C. The corresponding v_e histograms were similar for Capan-2 tumours and for CK-160 tumours, implying no change in v_e values when treated with Losartan for these tumours.

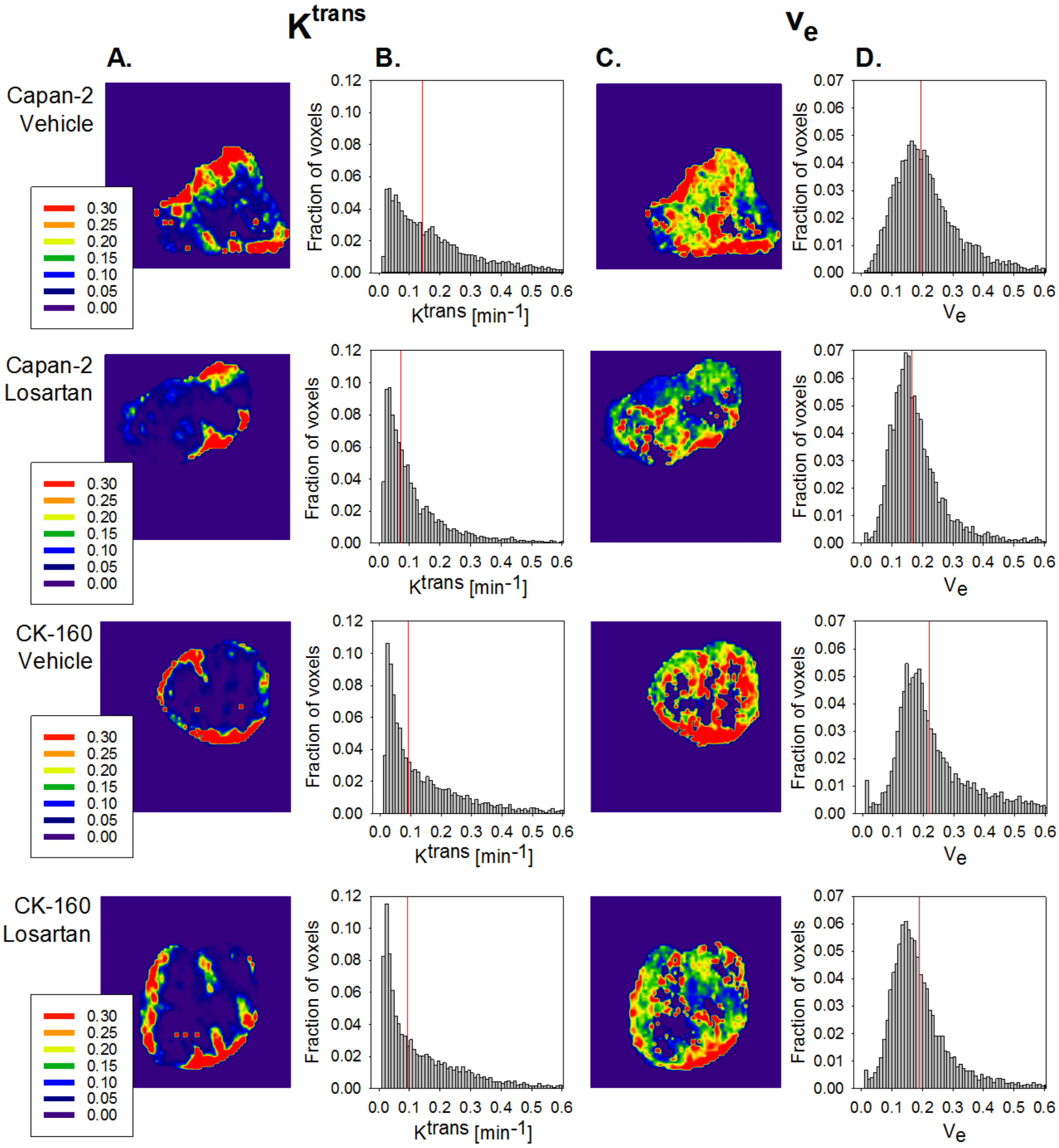

Figure 4.5: The figure shows K^{trans} (**A**) and v_e (**C**) images for representative tumours sections of both Losartan-treated and non-treated Capan-2 and CK-160 tumours. Column **B** and **C** show K^{trans} and v_e histograms of the tumours. The abscissa shows K^{trans} or v_e values, and the ordinate shows the fraction of these values in the tumours. Values for K^{trans} $[min^{-1}]$ and v_e [fraction] are shown by colour scale in the legend.

The average values of the populations are given in Figure 4.6, along with standard error represented by error bars. The Losartan treated Capan-2 tumour from Figure 4.5 showed reduced K^{trans} compared to the untreated tumour. This was also true for the entire population of Capan-2 tumours, showing a trend towards a reduction in K^{trans} values (**P >0.05** (0.09)) when treated with Losartan, as shown in Figure 4.6A. The trend towards reduced K^{trans} for tumours treated with Losartan was unexpected since Capan-2 tumours showed a similar trend towards a reduced hypoxic fraction, as displayed in Figure 4.2C. v_e values of Capan-2 populations correspond with the single tumours in Figure 4.6, with Figure 4.6B showing no difference in v_e (**P >0.05**) between untreated and Losartan-treated tumours.

Physiological parameters K^{trans} and v_e estimated from CK-160 tumours are displayed in Figure 4.6 C and D. These plots show no increase of either K^{trans} (**P >0.05**) or v_e (**P >0.05**) for tumours treated with Losartan. This corresponds with the results for histological images where there was no reduction in hypoxia for CK-160 tumours treated with Losartan, as displayed in Figure 4.2D.

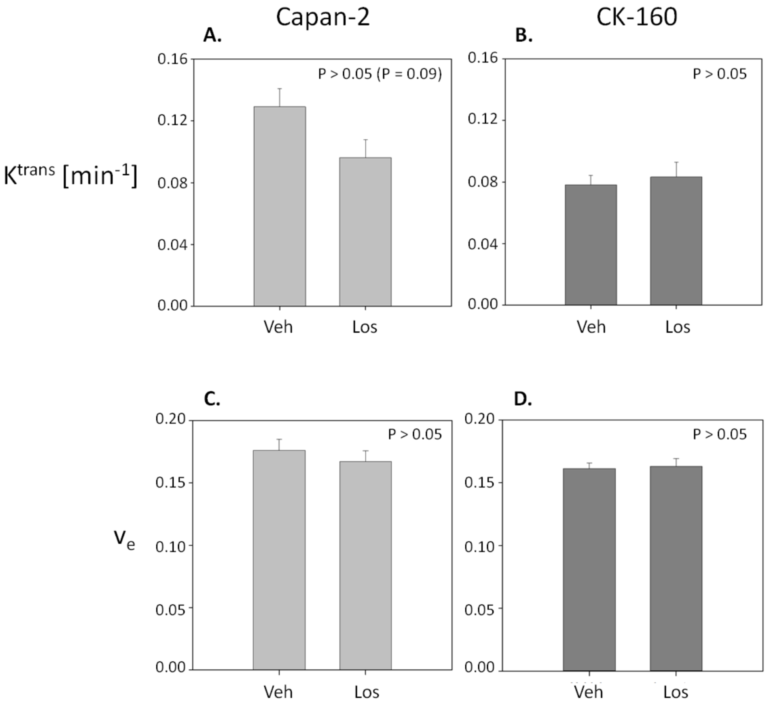

Figure 4.6: Top row shows K^{trans} values for Capan-2 tumours (**A**) and CK-160 tumours (**B**) of untreated (Veh) and Losartan-treated (Los) tumours. Bottom row shows v_e values for Capan-2 tumours (**C**) and CK-160 tumours (**C**). Bars show mean of 5 Capan-2 Veh, 9 Capan-2 Los, 9 CK-160 Veh, and 10 CK-160 Los. Error bars show standard error.

Capan-2 tumours treated with Losartan showed a trend towards a reduction in perfusion, demonstrated by K^{trans} values in Figure 4.6A. To see if there was a significant difference in distribution for K^{trans}, as there was for hypoxic fraction, a cumulative plot was estimated. Figure 4.7A, shows that there was a significant negative displacement of K^{trans} values in Losartan treated Capan-2 tumours ($P = \mathbf{0.0013}$). A P-value of 0.001, gives a clear indication that Losartan treatment, despite a reduction of the hypoxic fraction, reduced the blood flow of Capan-2 tumours. CK-160 tumours treated with Losartan showed no significant increase in perfusion ($P > \mathbf{0.05}$) in Figure 4.7B.

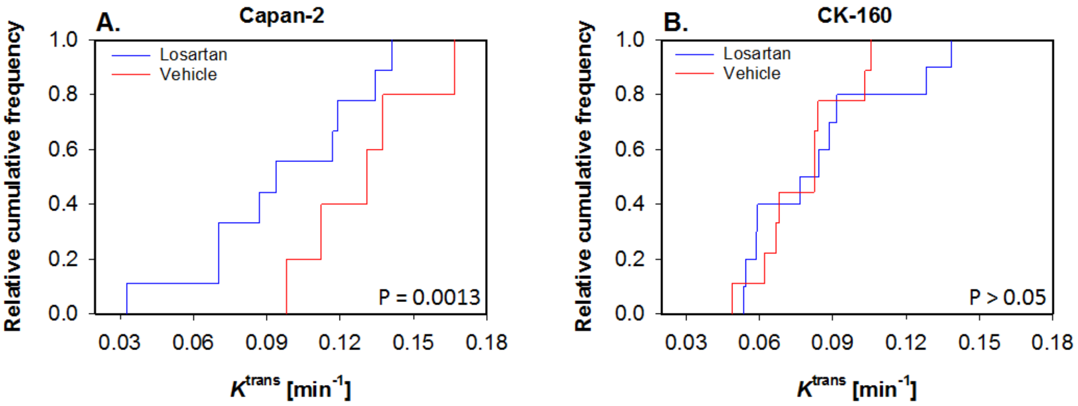

Figure 4.7: The cumulative plot for K^{trans} in Capan-2 tumours (**A**) and CK-160 tumours (**B**) are shown.

High levels of hypoxia is shown to correspond with low levels of perfusion [15]. Hence, the results from Capan-2 tumours, where the population treated with Losartan showed lower values of both hypoxia and K^{trans}, were surprising. To see if the hypoxic fraction and K^{trans} were correlated within the Capan-2 population, a scatter plot is shown in Figure 4.8. A linear fit based on the scatter plot of the treated and non-treated groups is also displayed in Figure 4.8. The linear fit shows good correlation for the Vehicle group ($R^2 = 0.83,\ P = 0.03$) and for the Losartan-treated group ($R^2 = 0.49,\ P = 0.04$). Within both groups, high K^{trans} values corresponded to low hypoxic fraction and low values of K^{trans} corresponded to high hypoxic fraction.

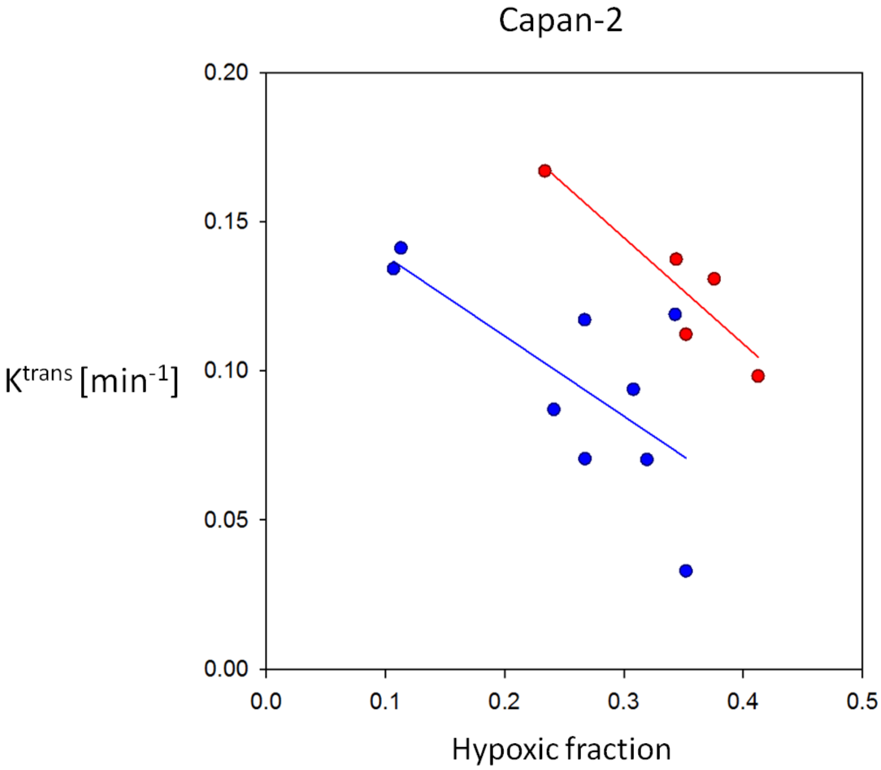

Figure 4.8: Correlation plot between the hypoxic fraction and the median K^{trans} value for individual Capan-2 tumours. It shows significant correlation within Losartan-treated ($R^2 = 0.49,\ P = 0.04$) and untreated groups ($R^2 = 0.83,\ P = 0.03$).

4.4 Fibrous content

Studies have shown that Losartan reduce collagen content, leading to a normalised TME and an increase in oxygenation [9]. Immunohistochemistry with collagen I antibody staining was therefore performed to investigate Losartan's anitfibrotic effect on Capan-2 and CK-160 tumour models.

Histological samples from both cancer models were analysed and the results are presented in Figure 4.9 alongside the mean values from the individual populations. For Capan-2 tumours, the collagen I antibody did not work properly, and the new antibody did not arrive in time. Collagen I content in Capan-2 tumours was therefore not estimated. Connective tissue fraction from the other histological images (Pimonidazole and HE) was used instead. The bright, pink bands in Figure 4.9A is connective tissue and was used to estimate the connective tissue fraction. Figure 4.9C shows no significant reduction in connective tissue for tumours treated with Losartan (**P >0.05**).

CK-160 tumours stained with collagen I antibody are presented with a representative untreated and Losartan treated tumour in Figure 4.9B. These images show similar amounts of collagen I displayed in brown, with similar distribution. This is also expressed by the untreated and Losartan treated groups in Figure 4.9D showing no difference in collagen I content between the groups of CK-160 tumours (**P >0.05**).

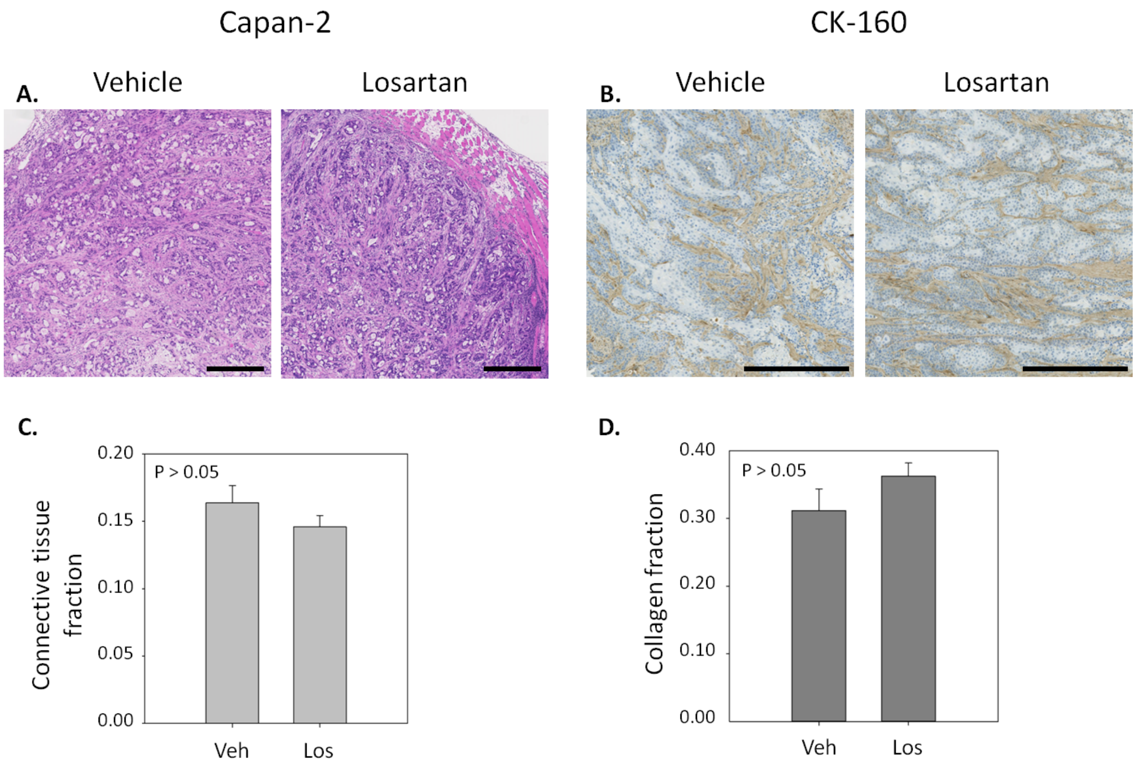

Figure 4.9: Connective tissue and collagen I fraction in representative Capan-2 (**A**) and CK-160 (**B**) tumours. **A** shows HE stained histological Capan-2 sections, used for calculating connective tissue fraction. **B** shows histological CK-160 sections stained with Collagen I antibody, used to calculate collagen fraction. Scale bar 0.5 mm. *C* shows connective tissue fraction of Capan-2 tumours and *D* shows collagen I fraction of CK-160 tumours. Bars show mean of 5 Capan-2 Veh, 9 Capan-2 Los, 7 CK-160 Veh, and 7 CK-160 Los. Error bars show standard error.

4.5 DW-MRI

The ADC is estimated by linear fit of the signal intensity for different b-values, where b-values decide the influence of diffusion in the imaging sequence. Examples of how ADC was estimated are shown in Figure 4.10A for a Capan-2 tumour and 4.10B for a CK-160 tumour. Figure 4.10A and B shows that it was possible to distinguish voxels with high ADC values from voxels of low ADC values based on the slope of the linear fit.

The tumours have not been affected by too much noise, shown by a decent signal-to-noise ratio for the individual lines and a sufficient linear fit for each voxel with R^2 values of 0.88 or larger. The different voxels shown in Figures 4.10A and 4.10B are marked with white arrows in the ADC images of Figure 4.10C and 4.10C.

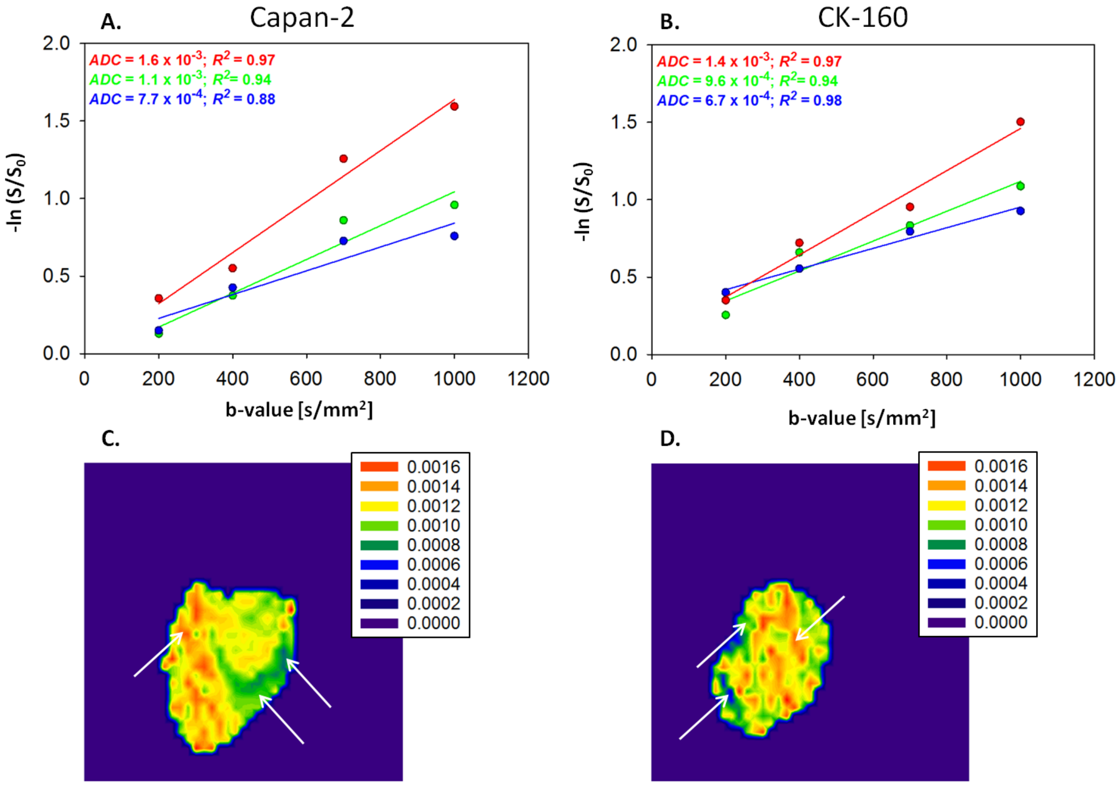

Figure 4.10: Signal intensity as a function of b-values for three different voxels from a representative Capan-2 tumour (**A**) and CK-160 tumour (**B**). The ADC values are given by the slope of the linear fit. Values of the individual voxels are shown, together with R^2, in the top left corner of the figures. The voxel displayed in **A** and **B** are marked by white arrows in ADC images of the Capan-2 tumour (**C**) and the CK-160 tumour (**D**). Values for ADC [s/mm^2] are shown by colour scale in the legend.

Representative Capan-2 and CK-160 tumours are displayed in columns A (Vehicle) and C (Losartan) in Figure 4.11. The distribution of ADC values of these tumours are displayed in histograms of Figure 4.11B (Vehicle) and 4.11D (Losartan). The top row of Figure 4.11 shows Capan-2 and the bottom row shows CK-160. High values of ADC reflect high levels of diffusion, and has previously been shown to correlate with a low fraction of collagen [23]. The ADC images of Figure 4.11 show that ADC values were scattered with high and low values both central and peripheral in the tumour.

The distribution of ADC values, shown by histograms in Figure 4.11B and D, shows that the majority of voxels contained ADC values between 0.5 and 1.5 10^{-3} mm^2/s. The mean values of the tumours were approximately 1.0 10^{-3} mm^2/s for both Capan-2 and CK-160 tumours.

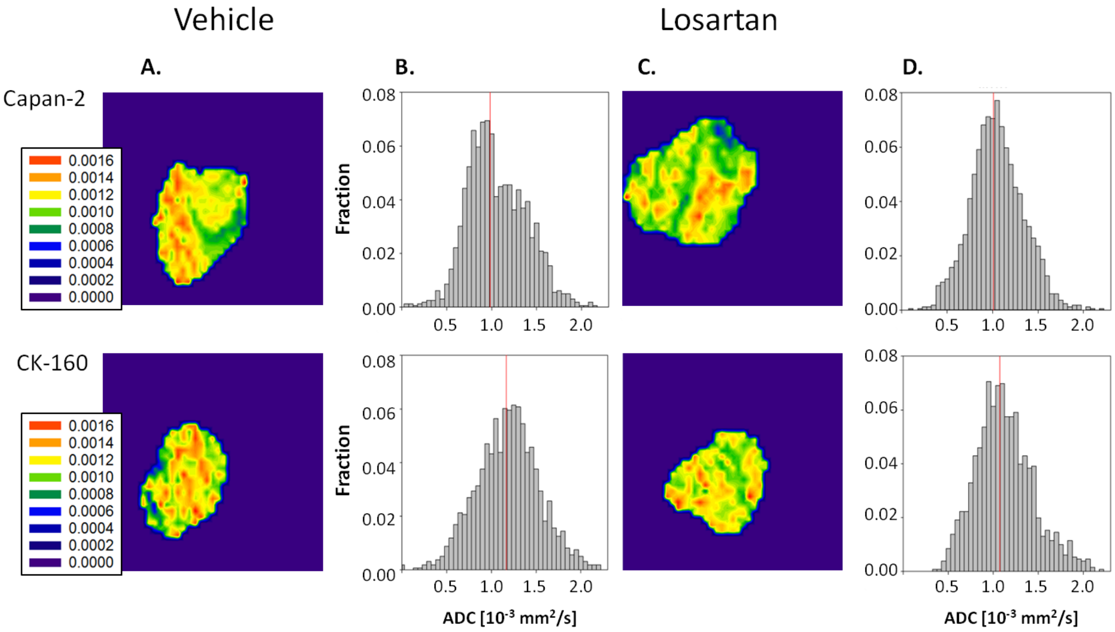

Figure 4.11: The figure shows representative tumours from Losartan-treated and non treated Capan-2 (top row) and CK-160 (bottom row) tumours. **A** shows ADC images of a section from vehicle tumours and **B** shows the ADC histogram in these tumours. **C** and **D** show equivalent plots for Losartan-treated tumours. Values for ADC [s/mm^2] are shown by colour scale in the legend.

The histograms for the Losartan-treated and Vehicle tumours were fairly similar for both cancer models. This corresponds with the mean values of ADC for untreated and Losartan-treated tumours of Capan-2 and CK-160 shown in Figure 4.12. Capan-2 tumours showed no difference between untreated and Losartan treated tumours (**P >0.05**) as illustrated in Figure 4.12A. Losartan treatment did not affect ADC levels of CK-160 tumours either (**P >0.05**).

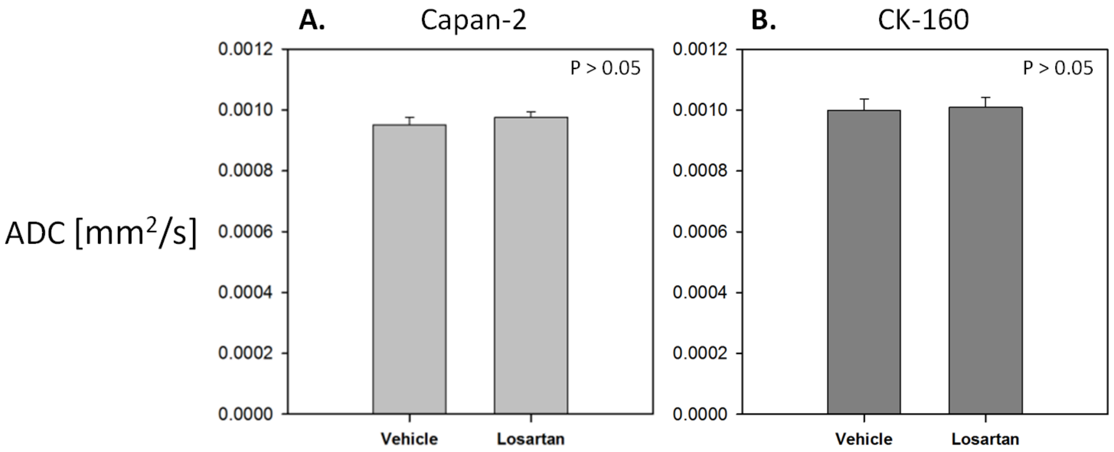

Figure 4.12: ADC values of untreated (Veh) and Losartan-treated (Los) Capan-2 tumours (**A**) and CK-160 tumours (**B**). Bars show mean of 5 Capan-2 Veh, 9 Capan-2 Los, 9 CK-160 Veh, and 10 CK-160 Los. Error bars show standard error.

Chapter 5

Discussion

The goal of this study was to investigate the use of Losartan to increase oxygenation in a cervical tumour model and a PDAC tumour model, by decreasing collagen I content and increasing perfusion. Losartan did not affect collagen I content, hypoxia or perfusion CK-160 tumours, but reduced both perfusion and hypoxic content in Capan-2 tumours without affecting connective tissue fraction.

This section will start with discussing the material and methods, followed by discussing the treatment effect and end with suggesting future investigations.

5.1 Materials and method

5.1.1 Mice and cancer models

Xenografts

The histological characteristics of the original tumour are usually maintained when the cells are established as tumours in mice [22]. However, the stromal tissue and vascular network is of mouse origin [16][22]. This could affect the response and characteristics of tumours compared to the donor tumour, but studies show that fundamental biological properties of the donor tumour are retained after xenotransplantation [16]. These biological properties include histology, growth pattern and response to treatment. The tumour growth rate of xenografts in mice are higher, with a doubling time five times shorter than if the tumour would have grown in humans [22].

In the current study the cervical tumour model CK-160 and the PDAC model Capan-2 was used to investigate the effect of Losartan treatment. Ellingsen et al. [16] showed that CK-160 xenografts reflected the histological appearance of donor patients tumours. The xenograft tumours showed heterogeneity between tumours in hypoxic fraction, interstitial fluid pressure and pH. CK-160 also showed substantial levels of collagen content [25]. These factors make it a valuable preclinical model for studies of the physiological micro-environment [16]. Capan-2 xenografts are also shown to have substantial levels of hypoxia and collagen I [48][49]. The tumor models CK-160 and Capan-2 should therefore be well suited for investigating whether Losartan treatment can increase oxygenation by reducing collagen content.

Studies comparing PDAC and cervical carcinoma xenografts showed that both types developed substantial stroma, but the connective tissue was more extensive and the density of collagen fibres was higher in PDAC than in the cervix carcinoma xenograft [49]. In the PDAC xenografts, more of the vessels were located in the connective tissue than the tumour parenchyma, compared to the cervical cancer models [49]. These differences could influence the tumour models response to Losartan treatment.

Unpublished studies within the research group, measured the effect of Losartan with MRI for different tumour volumes and showed that 400 mm^3 was the optimal volume. Hence, for the current study tumours were imaged and extracted when they reached a volume of 400 mm^3.

The cells of the innate immune system express mitogenic, angiogenic, stromal growth factors, as well as matrix remodelling enzymes when involved in wound healing [30]. This is an example of how inflammation, angiogenesis and desmoplasia is related. The use of immunodeficient athymic mice may influence the interaction between fibrosis, hypoxia and pathways related to the renin angiotensin system. Effects of Losartan treatment obtained in immunodeficient mice should be validated in mice with a fully functional immune system before the treatment strategy is tested in patients.

Losartan dose

When choosing the dose for Losartan treatment, there are two issues that need to be taken into consideration. The dose needs to be large enough that it affects fibrosis, but small enough that it does not affect the systemic blood pressure. In several studies, 40 mg/kg Losartan has been used [9][43][53] and did not decrease the systemic blood pressure [9]. Tang et al. [43] showed that daily treatment of 40 mg/kg for seven days was needed to affect the depletion of collagen content in breast cancer 4T1 xenograft model.

However, Diop-Frimpong et al. [13] measured the effect of Losartan using doses of 10, 20 and 60 mg/kg per day, and found a significant reduction in collagen using 20 mg/kg. In this study, 60 mg/kg Losartan had the most prominent effect on collagen I content, but had an impact on the systemic blood pressure of the mice. A daily treatment of 20 mg/kg also showed a significant reduction in collagen content for both tumour models used [13]. The current study used a daily treatment with 30 mg/kg of Losartan which should be sufficient for depleting collagen I without affecting the systemic blood pressure.

Blending Losartan and PBS was challenging, and the container had to be shaken before each injection. The injection was made with a syringe, and all of the mixture should have been injected. However, as the mixture was not fully homogeneous, there could be varying traces of Losartan left in the syringe. It is possible that this affected the actual injected dose, resulting in some mice receiving a smaller injection than planned. However, a study by Diop-Frimpong et al. [13] showed a significant decrease of collagen I content with a dose of 20 mg/kg. Even if there were small amounts of Losartan left in the syringe, it would not be enough to result in a dose lower than 20 mg/kg.

If traces of Losartan remained in the syringe, this could have been added to the injection of the next mouse. However, there is no reason to believe that this dose would surpass 40 mg/kg either. Due to the small size of the potential variation in dose, compared to the length of the treatment period, the uncertainty in regard of blending the mixture should not influence the results. Also, the mice were randomly chosen when injected with Losartan, which reduced the chance of treating individual mouse systematically with a lower or higher dose than intended.

5.1.2 DCE-MRI

A Fast Spin Echo sequence was used for creating the R_0^1-map. In the MR protocol, all FSE sequences had a slice thickness of 0.7 mm and a gap of 0.3 mm. When the RF-pulse excites a slice in the tumour, and if the neighbouring slices are too close, parts of the neighbours will be excited as well. The sequence assumes that the magnetisation is in equilibrium before the next excitation, which is not correct if the surrounding slices still are excited from the last pulse. This is called cross-excitation and affects the image contrast. Hence, a gap between the slices of at least 20-30% is recommended [7]. The FSE sequence was also used for the diffusion weighted imaging and the initial anatomical T_2 sequence.

Data from the DCE-MRI was analysed using Tofts pharmacokinetic model, which uses the measured concentration of contrast agent in tissue to estimate physiological parameters for perfusion and interstitial volume fraction. The pharmacokinetic Tofts model has been shown to provide a good fit for Gd-DOTA concentrations-versus-time curves for single voxels in vascularised tissue [49]. However, the Tofts pharmacokinetic model breaks down in voxels of poorly and non-vascularised tissue. The voxels containing this type of tissue have $v_e > 1$ and often higher than 1000 [49]. Wegner et al. [49] showed that these areas are related to necrotic and/or fibrotic tissue. This made it necessary to exclude these voxels when estimating frequency distribution and median values of K^{trans} and v_e for CK-160 tumours in this study.

When creating the R_0^1-map, Equation 2.25 was used with varying TR (TR $\leq$ 5000 ms). Equation 2.25 implies that low values of R_1 use longer time to reach equilibrium and that high values of TR are needed. Smistad et al. [39] showed that the accuracy when calculating R_1 values based on TR of 15000 ms was not substantially higher compared to 5000 ms. TR values of 200-5000 ms were chosen in the current study to save time and avoid the mice staying anaesthetised for longer than necessary.

Arterial input function

An Arterial input function is needed in the Tofts pharmacokinetic model when calculating K^{trans} and v_e. The AIF describes the diffusion of contrast agent from the blood vessels to the tissue and the excretion of contrast agent to the kidneys [3]. Instead of using individually adapted arterial input functions for each mouse, it was assumed that the same function was applicable for all mice. Benjaminsen et al. [3] showed that this is a fair assumption for genetically identical athymic mice. For human patients, individual AIFs should be estimated when using DCE-MRI and the Tofts pharmacokinetic model.

To achieve equal amount of contrast agent in the mice, the amount injected was adapted to the weight of the mouse, giving 5 ml/kg. With a constant infusion rate of 0.037 ml/s the injection time varied between the mice due to differences in weight. The mice weighed between 24 g and 34 g, resulting in injecting times varying between 7.6 s and 11 s. The time resolution of the DCE-MRI was 14.8 s, so the difference in injecting times was small compared to the time resolution. The variation in injection times should therefore not affect the imaging results. Since the infusion was made with an injection pump, the uncertainties regarding the infusion rate was negligible.

The AIF assumes that all of the contrast fluid is injected into the vein of the tail. To be sure this was the case, Smistad et al. [39] found a threshold based on the relationship of the signal intensity in the muscle before and after injection of contrast agent.The threshold was used in the current study to separate cases with or without sufficient uptake of contrast fluid. Tumours that did not surpass this threshold was discarded from the DCE-MRI analysis.

5.1.3 DW-MRI

ADC reflects the movement of water in tissue, and low ADC values imply obstructed movement [4]. Since the imaging sequence is sensitive to the movement of the water within the body, it is also susceptible to the movement of the body [4]. The mouse was therefore anaesthetised and fixated during the imaging sequence. However, due to movement when breathing there was still some noise in several of the images.

To prevent noise, the voxel size was larger for the FSE DW-MRI sequence, than for the other sequences. This was done since the signal to noise ratio is proportional to the size of the voxels [4]. Also, signal intensities were measured in three perpendicular directions for each voxel, and the average signal intensity of these directions was used when estimating ADC and R^2 values.

The b-values of the imaging sequence were between 200-1000 s/mm^2, to only detect extracellular movement [23]. b-values lower than 150 s/mm^2 results in blood perfusion being interpreted as diffusion, and intracellular diffusion are detected when using b-values higher than 1000 s/mm^2 [39].

Median ADC values may be influenced by areas of necrosis in CK-160 tumours [25]. This could be compensated for by removing voxels with v_e-values larger than one when estimating median ADC in CK-160 tumours. However, since there was no difference in collagen I content between untreated and Losartan treated tumours, removing voxels of $v_e > 1$ should not influence the estimated ADC. Also, v_e is affected by fibrosis in addition to necrosis, and it was therefore not certain if removing v_e values larger than one would improve the accuracy of ADC. Capan-2 showed no signs of necrotic tissue or any difference in connective tissue content between Losartan treated and untreated tumours, and should therefore not be affected by removing voxels of $v_e > 1$ either.

MRI - Image analysis

MR images was analysed as fast as they were taken. This made it hard to achieve a random analysis of the tumours, which can prevent conformation bias. However, the only step that involved human influence was the drawing of ROIs, which was done as consistently as possible and repeated at least once to confirm the results.

The MR images was imported to Matlab as DICOM files. The images were analysed based on a ROI drawn around the periphery of the tumour sections. In some tumour sections there were areas that were hard to distinguish between normal tissue and tumour tissue. Median values of K^{trans}, v_e and ADC values may vary with how the regions were drawn. Especially K^{trans} values have been shown to be higher for voxels along the periphery [3]. All tumour ROIs were therefore drawn ate at least twice to confirm consistency. CK-160 tumours, which were analysed first, required some training for a decent analysis. However, the repeated analysis did not show any substantial deviations between ROI delineations.

5.1.4 Immunohistochemistry

For the immunohistochemistry analysis of hypoxia, necrosis and collagen I, only one section of each tumour was used, derived from the middle of the tumour. There are variations within the tumour, and if the fractions had been calculated based on sections from the entire tumour, the result could have looked differently.

Previous studies with DCE-MRI showed that the K^{trans} and v_e frequency distribution derived from the central axial section, were similar to the ones derived from the entire tumour [15]. It is therefore reasonable to assume that the midsection of a tumour gives good indication of the overall condition of the tumour, for histological samples as well.

Image analysis

Histological tumour images were analysed in two bulks, one for all CK-160 tumours and one for all Capan-2 tumours. Within the bulks, the tumours were chosen as randomly as possible when analysed. This was to avoid analysing Losartan treated or untreated tumours first, giving one group a higher uncertainty than the other. It was also to limit conformation bias during data analysis.

The histological images were imported to ImageJ. Hypoxia, necrosis, collagen I and connective tissue was estimated using ROIs or counting of vertices. ROIs and counting vertices is somewhat prone to human errors. When evaluating areas of hypoxia, consistency regarding the limits for hypoxic, necrotic and normoxic areas was occasionally difficult to achieve. The immunohistochemistry colour staining also varied between the sections, and sections had to be evaluated individually instead of using a universal threshold. A universal threshold was tested, but small variations in the threshold resulted in large variations in the estimated fraction, and the method was discarded. The analysis was repeated at least once for each images to obtain highest possible accuracy.

The necrotic areas of CK-160 tumours were visible in all three types of histological images, and area estimates was therefore easy to compare between the image types.

The collagen I antibody staining did not work when staining Capan-2 tumours, and this was confirmed by insufficient staining of the positive control. The new antibody did not arrive in time and collagen I content in Capan-2 tumours was therefore not investigated. Instead, the connective tissue fraction was estimated using the two other available histological image types instead. These were not stained for connective tissue, so the pattern and colour nuances of the areas had to be evaluated manually. Some areas stood out clearly as connective tissue, while others were harder to evaluate. There is therefore some uncertainty related to this procedure.

Analysed samples of MR-images and immunohistochemistry images were confirmed by more experienced personnel, such as Dr. Jon-Vidar Gaustad.

5.2 Treatment effect

Previous studies have shown that Losartan reduces collagen content in tumours and thereby reduces solid stress [9]. This reduction in solid stress relieves compression force on blood vessels and increase perfusion which ultimately increased oxygenation in the tumours [9]. This effect have been extensively studied in PDAC and breast cancer models, and similar effects have also been shown in skin and ovarian cancer models [9][13][43][53].

5.2.1 Capan-2

Capan-2 is a PDAC model. Previous studies by Diop-Frimpong et al. [13], Kumar et al. [26] and Chauhan et al. [9] all made use of PDAC models when studying the effects of Losartan. Even though these studies did not investigate the Capan-2 model, similar results with increased perfusion and reduced fibrous content were expected for Capan-2 tumours.

Losartan did reduce hypoxia in Capan-2 tumours, but also showed reduced values of K^{trans}. This implies that Losartan increased oxygenation, as for previously studied PDAC models. However, it also implies that the increase in oxygenation was not a result of increased perfusion, and that Losartan increased oxygenation by a different mechanism in Capan-2 tumours.

The level of oxygen is dependent on oxygen supply and oxygen consumption [15]. Losartan did not increase oxygen supply, but may have reduced oxygen consumption. It is possible that Losartan treatment affect the metabolism of tumour cells, but this is only speculations since the current study was not designed to measure effects in metabolism. It would therefore be interesting to design new experiments to study the effect of Losartan in metabolism and oxygen consumption.

It would also be interesting to study vessel walls of Capan-2 to investigate why perfusion is reduced by Losartan treatment. This could be done by colouring endothelial cells with CD31, which is used in immunohistochemistry to visualise blood vessels [49]. Endothelial cells are flattened cells that form a sheet inside the walls of vessel [1] This could be used to see if there are any structural differences in blood vessels between Losartan treated and untreated tumours. It has previously been reported that Losartan did not affect the production of blood vessels (angiogenesis) or the blood vessels density in other tumour models [9]. This, however, could be different in Capan-2 tumours.

5.2.2 CK-160

CK-160 is a cervical carcinoma model. The effect of Losartan has not been previously studied in cervical carcinoma models, despite tumours of cervical carcinomas showing substantial levels of hypoxia and collagen I [10][29].

Losartan did not reduce hypoxic fraction in CK-160 tumours. Losartan did not change perfusion or collagen I content in the tumours either, which implies that Losartan does not have an effect in CK-160 tumours. Since CK-160 is a cervical carcinoma model, the results indicate that Losartan does not work for cervical carcinomas. Similar studies of other cervical carcinoma models should be conducted to validate this.

However, Losartan did reduce necrotic fraction in CK-160 tumours. Tissue that remain hypoxic for long periods turn necrotic, if not re-oxygenated [22]. The reduction of necrotic fraction for CK-160 tumours treated with Losartan may therefore imply that oxygenation was increased. If this is the case, the mechanisms responsible for increased oxygenation not is due to increased supply of oxygen, since perfusion was not increased in CK-160 tumours.

The mechanism behind reduced necrosis in CK-160 tumours are unknown. Necrosis is related to hypoxia, and hypoxia was reduced in Capan-2 tumours without increasing perfusion. Hence, it is possible that the same mechanisms were involved in CK-160 tumours, and that the reduction in necrotic tissue was due to reduced oxygen consumption caused by changes in metabolism. There are, however, other mechanisms than ATP depletion involved in programmed necrosis such as disturbance of Ca^{2+} homeostasis, mitochondrial depolarisation and glucose depletion [33][37]. It would therefore be interesting to design new experiments to investigate if Losartan changes the metabolism and oxygen consumption of CK-160 tumours or if the reduction in necrotic fraction is due to other mechanisms.

5.2.3 Collagen I and connective tissue

Losartan has been shown to to be an inhibitor of collagen I synthesis [13]. However, Losartan did not affect collagen I levels in CK-160 tumours or connective tissue content in Capan-2 tumours. Two factors that was not assessed in this study was collagen cross-linking and orientation of collagen fibrils. The orientation can be of importance, as it could be used as a biomarker for tumour cell invasion, metastasis and poor outcome.

Cross-linked collagen is shown to increase stromal stiffness and confer proteolytic resistance [31]. Proteolysis is the degradation of proteins [1]. If collagen I in CK-160 and Capan-2 tumours was cross-linked in a manner that resist proteolysis, the prevention of collagen synthesis alone may not be sufficient to substantially reduce collagen I content. However, whether Losartan also affects collagen I degradation or not, needs to be investigated further.

5.3 Clinical relevance

Losartan treatment did not reduce collagen I content, did not increase perfusion and did not reduce hypoxia in CK-160 tumours. Hence, Losartan appears to not influence all cancer models in the same beneficial way. Since CK-160 is a cervix-model, this could imply that Losartan treatment does not have an affect in cervical cancer. New studies of different cervix-models are needed to confirm this. However, necrotic fraction was reduced, which may be due to increased oxygenation. Tumour necrosis is associated with poor prognosis [37] and if Losartan reduces necrosis in cervical cancer models, it could potentially improve the prognosis of cervical carcinoma patients. New preclincal studies should be designed to investigate the effect of Losartan on tumour necrosis, and to investigate whether a reduction in necrosis is beneficial.

Losartan reduced hypoxia in Capan-2 tumours. The reduction in hypoxia was, however, not caused by an increase in perfusion since K^{trans} was reduced. Losartan did not affect connective tissue content. The results of Losartan treatment in Capan-2 tumours indicate that Losartan may reduce hypoxia by a different mechanism than increased perfusion. This mechanism is not known, and new studies should be designed to find this mechanism. Hypoxia leads to malignant progression, an increased risk of metastasis as well as a resistance to radiotherapy and chemotherapy. Hence, Losartan may increase the survival rate of cancer patient, even though the mechanisms behind reduced hypoxia is not increased perfusion.

5.4 Future work

5.4.1 Increasing amount of data

Since immunohistochemistry was analysed on solely the midsection of the tumour, analysing additional sections of each tumour could be useful to examine variations within the tumour. Analysing additional tumours would also increase the impact of the result, especially for vehicle tumours of Capan-2, where only five tumours were sufficiently established. Nonetheless, the significant reduction in hypoxia and K^{trans} for Losartan treated Capan-2 tumours was estimated using Students t-test which takes the number of samples into consideration.

5.4.2 Immunohistochemistry

The estimation of collagen I content in Capan-2 tumours will take place as soon as the new antibody has arrived. The indications made by the estimated connective tissue fraction and ADC can not be confirmed until this is done.

Further studies to investigate if the orientation of collagen I fibrils influence the effect of Losartan could also be of interest. As of now, there has not been developed an automatic method to investigate the orientation, thickness and cross-linking of collagen fibrils. Evaluating it manually would be a time consuming process, and is the reason why fibril orientation has not been investigated in this study.

Immunohistochemistry staining for detecting hyaluronan could have been conducted in this study. However, Chauhan et al. [9] showed that collagen correlates inversely with perfusion regardless of hyaluronan levels. This is not the case for hyaluronan which is only correlated with reduced perfusion in tumours containing high levels of collagen I. Since oxygenation via increased perfusion was the most central issue for this study, staining with a collagen I antibody was considered sufficient. However, hyaluronan has been described as an important component in desmoplasia and reduced perfusion and hyaluronan could potentially play a different role in CK-160 and Capan-2 tumours. It should be investigated if hyaluronan content in CK-160 and Capan-2 tumours was affected by Losartan treatment, even though collagen I or connective tissue content was not affected. The role of hyaluronan in cancer initiation and progression makes it an important component in cancer and it should be studied further [31].

In addition to CD31, α-Smooth Muscle Actin (α-SMA) can be used to investigate the reduction in perfusion for Capan-2 tumours treated with Losartan. α-SMA is used as a marker for active CAFs and has previously been shown to be reduced in tumours treated with Losartan [9]. In addition to its relation to CAFs, a decrease in the expression of α-SMA in cells surrounding vasculature might suggest that vessels are fragile and immature [45]. Fragile and immature vessels may influence the perfusion in the tumours. The levels of α-SMA could therefore be used for further understanding of the reduced perfusion in Losartan treated Capan-2 tumours.

5.4.3 MRI

Even though the protocol used in this study has been shown to a good model for detecting collagen and diffusion, DW-MRI contains substantial noise. A new protocol is under development at the MRI Core facility at the Norwegian Radium Hospital which measures breathing, and times the image acquisitions to the intervals between respiration. This substantially reduces the noise in the image. For future studies, an implementation of this protocol could be beneficial.

Due to the implications contrast agents have for patients with reduced kidney function and the potential implications for the brain, exploring the use of improved DW-MRI sequences for detecting hypoxia could be of interest [21][34]. It would also be important to exploit the use of established DCE-MRI protocols with new and safer contrast agents.

5.4.4 Data science

Using machine learning and image analysis to evaluate traits of MRI images could be of great use in the future, when applied to DCE-MRI and DW-MRI. Using texture analysis, multiblock principal component analysis (PCA) and similar techniques to extract parameters of MRI images to predict physiological parameters, in combination with immunohistochemistry, could result in more effective methods and new parameters to reflect the condition of the tumours.

Also, it would be an advantage in histological images, to develop a universal threshold that works regardless of the colour intensity of the image. A problem when colour thresholds was attempted in this study was that small variations in the threshold resulted in large differences in the calculated hypoxic or collagen fraction. Using image analysis and machine learning to find a relative threshold based on the overall intensity of the image could be of great use. Throughout the years large amounts of tumour images have been analysed in preclinical studies, so the amount of data to base the analysis on, should be sufficient.

5.4.5 Investigating alternatives to Losartan treatment

Previous studies on the use of Losartan show promise for increasing perfusion in several tumour models [9]. Also, retrospective studies demonstrated that patients taking ARBs had decreased risk of developing some types of cancers [20]. This indicates that preventive use with Losartan, could have beneficial effects.

Even though Losartan is approved by the FDA and regarded as safe to use, there are side effects [32]. Several of them are common, most of them mild. However, for preventive use, there could be other methods than Losartan. In an interview with hypertension specialist Dr. Houston in 2014, alternative ways to treat hypertension were suggested [2]. The interview was based on review articles on nutrition and nutraceutical supplements for the treatment of hypertension. The articles investigates methods for replacing pharmaceuticals with nutritional alternatives and exercise to regulate the systemic blood pressure. It was suggested that several compounds with ARB qualities commonly found in diets such as potassium, Vitamin C, Coenzyme Q10 could be used.

Focusing on components which are already implemented in common diets could be desirable, due to the complexity of the Renin-Angiotensin system. Designing studies that explores the use of dietary compounds with ARB qualities could be of interest when investigating preventive measures.

Chapter 6

Conclusion

Tumours of the cervical cancer model, CK-160, did not show any signs of increased values of K^{trans} ($P > 0.05$) when treated with Losartan, implying that Losartan did not improve blood flow. There was no reduction in hypoxia ($P > 0.05$), but Losartan reduced the amount of necrotic tissue in the tumours ($P = 0.03$). There was no reduction in collagen I content ($P > 0.05$) for mice treated with Losartan, which was reflected by an absence of increase in ADC ($P > 0.05$). There was not sufficient evidence to support that Losartan improved oxygenation in CK-160 tumours.

Losartan treated Capan-2 tumours showed a significant reduction in hypoxic fraction for tumours treated with Losartan ($P = 0.007$). The reduction of hypoxia was not due to an increase in blood flow, since Losartan treated tumours also showed a reduction in K^{trans} ($P < 0.001$). Capan-2 tumours did not show necrosis. Collagen I content was not assessed, but the fraction of connective tissue in tumours was estimated. Losartan treated and non-treated tumours showed no significant difference in connective tissue fraction ($P > 0.05$), and could therefore not explain the reduction in perfusion of tumours treated with Losartan. There were clear indications that Losartan increased oxygenation in Capan-2 tumours, but this increase was not a result of an increase in blood flow. This implies that there are other mechanisms responsible for the increase in oxygenation that are not known, which needs to be investigated further.

Losartan increased oxygenation in Capan-2 tumours, but not in CK-160 tumours.

Bibliography

[1] Alberts, B., Johnson, A., Lewis, J., Raff, M., Roberts, K. and Walter, P. [2002], *Molecular biology of the Cell*, 4th edn, Garland Science - Taylor & Francis Group. Page 47-128, 767-830, 990-992, 1313-1363, 1367-1406, 1461-1462, G:6-14.

[2] Alexander, W. [2014], 'Hypertension: Is it time to replace drugs with nutrition and nutraceuticals', *Pharmacy and Therapeutics (P&T)* **39**(4), 291–295. Interview with Mark Houston, MD.

[3] Benjaminsen, I. C., Graff, B. A., Brurberg, K. G. and Rofstad, E. [2004], 'Assessment of tumour blood perfusion by high-resolution dynamic contrast-enhanced MRI: A preclinical study of human melanoma xenografts', *Magnetic resonance in medicine* **52**(2), 269–276. doi: 10.1002/mrm.20149.

[4] Bjørnerud, A. [2008], 'The physics of magnetic resonance imaging, kompendium II to the course FYS-KJM4740'.

[5] Bray, F., Ferlay, J., Soerjomataram, I., Siegel, R., Torre, L. and Jemal, A. [2018], 'Global cancer statistics 2018: GLOBOCAN estimates of incidence and mortality worldwide for 36 cancers in 185 countries', *CA: A Cancer Journal for Clinicians* **68**(6). doi: 10.3322/caac.21492.

[6] Brown, S. and Sneyd, J. [2015], 'Nitrous oxide in modern anaesthetic practice', *BJA Education* **16**(3), 87–91. doi: 10.1093/bjaceaccp/mkv019.

[7] Catherine Westbrook, C. K. R. and Talbot, J. [2011], *MRI in practice*, 4th edn, Wiley-Blackwell.

[8] Chan, M. [2016], 'Obesity and diabetes: the slow-motion disaster keynote address at the 47th meeting of the national academy of medicine'. Accessed October 9th, 2019.
URL: *https://www.who.int/dg/speeches/2016/obesity-diabetes-disaster/en/*

[9] Chauhan, V. P., Martin, J. D., Liu, H., Lacorre, D. A., Jain, S. R. and et. al, S. V. K. [2013], 'Angiotensin inhibition enhances drug delivery and potentiates chemotherapy by decompressing tumour blood vessels', *Nature Communications* **4**(2516). doi: 10.1038/ncomms3516.

[10] Cui, Y., Zhang, X., You, K., Guo, Y., Liu, C. and et al., X. F. [2017], 'Nanomechanical characteristics of cervical cancer and cervical intraepithelial neoplasia revealed by atomic force microscopy', *Medical Science Monitor* **23**, 4205–4213. doi: 10.12659/MSM.903484.

[11] Deer, E. L., Gonzalez-Hernandez, J., Coursen, J. D., Shea, J. E., Ngatia, J. and et al., C. L. S. [2010], 'Phenotype and genotype of pancreatic cancer cell lines', *NIH Public Access - Author Manuscript* **39**(4), 425–435. doi: 10.1097/MPA.0b013e3181c15963.

[12] Deroules, C., Ameisen, D., Badoual, A., Gerin, C., Granier, A. and Lartaud, M. [2013], 'Analyzing huge pathology images with open source software', **8**(92). doi: 10.1186/1746-1596-8-92.

[13] Diop-Frimpong, B., Chauhan, V. P., Krane, S., Boucher, Y. and Jain, R. K. [2011], 'Losartan inhibits collagen 1 synthesis and improves the distribution and efficacy of nanotherapeutics in tumors', *Procedings of the National Academy of Sciences of the United States of America (PNAS)* **108**(7), 2909–2914. doi: 10.1073/pnas.1018892108.

[14] Edinger, A. L. and Thompson, C. B. [2004], 'Death by design: apoptosis, necrosis and autophagy', *Current Opinion in Cell Biology* **16**(6), 663–669. doi: 10.1016/j.ceb.2004.09.011.

[15] Egeland, T. A., Gulliksrud, K., Gaustad, J.-V., Mathiesen, B. and Rofstad, E. K. [2012], 'Dynamic contrast-enhanced MRI of tumour hypoxia', *Magnetic Resonance in Medicine* **67**, 519–530. doi: 10.1002/mrm.23014.

[16] Ellingsen, C., Natvig, I., Gaustad, J.-V., Gulliksrud, K., Egeland, T. A. M. and Rofstad, E. K. [2009], 'Human cervical carcinoma xenograft models for studies of the physiological microenvironment of tumors', *Journal of Cancer Research and Clinical Oncology* **135**(9), 1177–1184. doi: 10.1007/s00432-009-0558-8.

[17] for Biotechnology Information PubChem Database, N. C. [n.d.], 'Tetraxetan - compound summary'. Accessed November 7th, 2019.
URL: *https://pubchem.ncbi.nlm.nih.gov/compound/Tetraxetansection=Depositor-Supplied-Synonyms*

[18] Gachon, F. and Firsov, D. [2010], ‘The role of circadian timing system on drug metabolism and detoxification’, *Expert Opinion on Drug Metabolism & Toxicology* **7**(2), 147–158. doi: 10.1517/17425255.2011.544251.

[19] Gaustad, J.-V., Simonsen, T. G., Smistad, R., Wegner, C. S., Andersen, L. M. K. and Rofstad, E. [2015], ‘Early effects of low dose bevacizumab treatment assessed by magnetic resonance imaging’, *BMC Cancer* .

[20] George, A. J., Thomas, W. G. and Hannan, R. D. [2010], ‘The rening-angiotensin system and cancer: old dog, new tricks’, *Nature reviews - Cancer* **10**(11), 745–759. doi: 10.1038/nrc2945.

[21] Guo, B., Yang, Z. and Zhang, L. [n.d.], ‘Gadolinium deposition in brain: Current scientific evidence and future perspectives.’, *Frontiers in Molecular Neuroscience* **11**(335).

[22] Hall, E. J. and Giaccia, A. J. [2018], *Radiobiology for the Radiologist*, 8 edn, Wolters Kluwer. Page 82-100, Page 458,461, Page 388-389.

[23] Hauge, A., Wegner, C. S., Gaustad, J.-V., Simonsen, T. G., Andersen, L. M. K. and Rofstad, E. K. [2017], ‘Diffusion-weighted MRI-derived ADC values reflect collagen I content in PDX models of uterine cervical cancer’, *Oncotarget* **8**(62), 105682–105691. doi: 10.18632/oncotarget.22388.

[24] Hauge, A., Wegner, C. S., Gaustad, J.-V., Simonsen, T. G., k. Andersen, L. M. and Rofstad, E. K. [2017], ‘DCE-MRI of patient-derived xenograft models of uterine cervix carcinoma: associations with parameters of the tumor microenvironment’, **15**(225), 544.

[25] Hompland, T., Ellingsen, C., Galappathi, K. and Rofstad, E. K. [2014], ‘Connective tissue of cervical carcinoma xenografts: Associations with tumor hypoxia and interstitial fluid pressure and its assessment by DCE-MRI and DW-MRI’, *Acta Oncologica* **53**(1), 6–15. doi: 10.3109/0284186X.2013.773073.

[26] Kumar, V., Boucher, Y., Liu, H., Ferreira, D., Hooker, J. and et al., C. C. [2016], ‘Noninvasive assessment of Losartan-induced increase in functional microvasculature and drug delivery in pancreatic ductal adenocarcinoma’, *Translational Oncology* **9**(5), 431–437. doi: 10.1016/j.tranon.2016.07.004.

[27] Leverve, X., Batandier, C. and Fontaine, E. [2007], ‘Choosing the right substrate’, *Novartis Foundation symposium* **280**, 108–21; discussion 121. doi: 10.1002/9780470059593.ch8.

[28] Li, X., Shepard, H. M., Cowell, J. A., Zhao, C., Osgood, R. J. and et al., S. R. [2018], ‘Parallel accumulation of tumor hyaluronan, collagen, and other drivers of tumor progression’, *Clinical Cancer Research* **24**(19), 4798–4807. doi: 10.1158/1078-0432.CCR-17-3284.

[29] Lu, Z. H., Wright, J. D., Belt, B., Cardiff, R. D. and Arbeit, J. M. [2007], ‘Hypoxia-inducible factor-1 facilitates cervical cancer progression in human papillomavirus type 16 transgenic mice’, *The American Journal of Pathology* **171**(2), 667–681. doi: 10.2353/ajpath.2007.061138.

[30] Martin, J. D., Fukumura, D., Duda, D. G., Boucher, Y. and Jain, R. K. [2016], ‘Reengineering the tumor microenvironment to alleviate hypoxia and overcome cancer heterogeneity’, *Cold Spring Harb Perspect Med* **6**(12). doi: 10.1101/cshperspect.a027094.

[31] McCarthy, J. B., El-Ashry, D. and Turley, E. A. [2018], ‘Hyaluronan, cancer-associated fibroblasts and the tumor microenvironment in malignant progression’, *Frontiers in Cell and Developmental Biology* **6**(48). doi: 10.3389/fcell.2018.00048.

[32] Merck Sharp Dohme Limited 2018 [n.d.], ‘Cozaar 2.5 mg/ml powder and solvent for oral suspension’. Accessed November 27th 2019.
URL: *https://www.medicines.org.uk/emc/product/6587/smpc*

[33] Moriwaki, K. and Chan, F. K.-M. [2013], ‘RIP3: a molecular switch for necrosis and inflammation’, *Genes and Development* **27**(15), 1640–1649. doi: 10.1101/gad.223321.113.

[34] Nicola Schieda and Jason I. Blaichman and Andreu F. Costa and Rafael Glikstein and Casey Hurrell and Matthew James et al. [2018], ‘Gadolinium-based contrast agents in kidney disease: Comprehensive review and clinical practice guideline numberd by the canadian association of radiologists’, *Canadian Association of Radiologists Journal* **69**(2), 136 – 150. doi: 10.1016/j.carj.2017.11.002.

[35] Perunovic, B. and Sunassee, A. [2018], ‘Squamous cell carcinoma’. Accessed October 10th, 2019.
URL: *http://www.pathologyoutlines.com/topic/cervixSCC.html*

[36] Pinter, M. and Jain, R. K. [2017], ‘Targeting the renin-angiotensin system to improve cancer treatment: Implications for immunotherapy’, *Science translational medicine* **9**(410). doi: 10.1126/scitranslmed.aan5616.

[37] Qiu, Y., Li, P. and Ji, C. [2015], 'Cell death conversion under hypoxic condition in tumor development and therapy', *International Journal of Molecular Science* **16**(10), 25536–25551. doi: 10.1101/gad.223321.113.

[38] Rawla, P., Sunkara, T. and Gaduputi, V. [2018], 'Epidemiology of pancreatic cancer: Global trends, etiology and risk factors', *World Journal of Oncology* **68**(6). doi: 10.3322/caac.21492.

[39] Smistad, R. [2014], Kan effekten av avastin detekteres med magnetisk resonansavbildning, Master's thesis, Norges miljø og biovitenskapelige universitet.

[40] Special diet service [n.d.], 'SDS info-sheet 050523'. Accessed November 7th 2019.
URL: *http://www.sdsdiets.com/pdfs/Irradiation.pdf*

[41] Stark, A., Eibl, G. and Geffen, D. [2015], 'Pancreatic ductal adenocarcinoma'. From the Department of Surgery - UCLA Center for Excellence in Pancreatic Diseases and School of Medicine at UCLA.

[42] Szadvari, I., Krizanova, O. and Babula, P. [2016], 'Athymic nude mice as an experimental model for cancer treatment.', *Physiological research* **65**(4), 441–453.

[43] Tang, Y., Liu, Y., Wang, S., Tian, Y. and Teng, Z. [2019], 'Depletion of collagen by Losartan to improve tumor accumulation and theurapeutic efficacy of photodynamic nanoplatforms', *Springer Nature* **9**(3). doi: 10.1007/s13346-018-00610-1.

[44] Tofts, P. S., Brix, G., Buckley, D. L., Evelhoch, J. L., Henderson, E. and et. al, M. V. K. [1999], 'Estimating kinatic parameters from dynamic contrast-enhanced T_1-weighted MRI of a diffusable tracer: Standardized quantities and symbols', *Journal of Magnetic Resonance Imaging* **10**(3), 223–232. doi: 10.1002/(sici)1522-2586(199909)10:3<223::aid-jmri2>3.0.co;2-s.

[45] Tonino, P. and Abreu, C. [2011], 'Microvessel density is associated with VEGF and α-SMA expression in different regions of human gastrointestinal carcinomas', *Cancers* **3**(3), 3405–3418. doi: 10.3390/cancers3033405.

[46] Voutouri, C., Polydorou, C., Papageorgis, P., Gkretsi, V. and Stylianopoulos, T. [2016], 'Hyaluronan-derived swelling of solid tumors, the contribution of collagen and cancer cells, and implications for cancer therapy', *NEOPLASIA* **18**(12), 732–741. doi: 10.1016/j.neo.2016.10.001.

[47] Webb, S. [2012], *Webb's physics of medical imaging*, 2nd edn, CRC Press - Taylor & Francis Group.

[48] Wegner, C. S., Gaustad, J.-V., Andersen, L. M. K., Simonsen, T. G. and Rofstad, E. K. [2016], 'Diffusion-weighted and dynamic contrast-enhanced MRI of pancreatic adenocarcinoma xenografts: associations with tumor differentiation and collagen content', *Journal of Translational Medicine* **14**(161). doi: 10.1186/s12967-016-0920-y.

[49] Wegner, C. S., Hauge, A., Gaustad, J.-V., Andersen, L. M. K., Simonsen, T. G., Galappathi, K. and Rofstad, E. K. [2017], 'Dynamic contrast-enhanced MRI of the microenvironment of pancreatic adenocarcinoma xenografts', *Acta Oncologica* **56**(12), 1754–1762. doi: 10.1080/0284186X.2017.1343494.

[50] Weinmann, H.-J., Brasch, R. C., Press, W.-R. and Wesbey, G. E. [1984], 'Characteristics of gadolinium-DTPA complex: a potential NMR contrast agent', *American journal of Roentgenology* **142**(3), 619–624. doi: 10.2214/ajr.142.3.619.

[51] Whatcott, C. J., Posner, R. G., Hoff, D. D. V. and Haiyong, H. [2012], *Pancreatic Cancer and Tumor Microenvironment.*, Trivandrum (India): Transworld Research Network. Chapter 8: Desmoplasia and chemoresistance in pancreatic cancer.

[52] WHO [2018], 'Press release N °263: Latest global cancer data'. Accessed October 10th, 2019.
URL: *https://www.who.int/cancer/PRGlobocanFinal.pdf*

[53] Zhao, Y., Cao, J., Melamed, A., Worley, M., Gockley, A. and Jones, D. [2018], 'Losartan treatment enhances chemotheray efficacy and reduces ascites in ovarian cancer models by normalizing the tumor stroma', *Procedings of the National Academy of Sciences of the United States of America (PNAS)* **116**(6), 2210–2219. doi: 10.1073/pnas.1818357116.

Norges miljø- og biovitenskapelige universitet
Noregs miljø- og biovitskapelege universitet
Norwegian University of Life Sciences

Postboks 5003
NO-1432 Ås
Norway